Three-Dimensional Modeling of the O2(1Δ) Dayglow: Dependence on Ozone and Temperatures

Mouhamadou Makhtar Ndiaga Diouf, Franck Lefèvre, Alain Hauchecorne, Jean-Loup Bertaux

JGR Atmospheres

RESEARCH ARTICLE
10.1029/2023JD040159

Three-Dimensional Modeling of the $O_2(^1\Delta)$ Dayglow: Dependence on Ozone and Temperatures

Mouhamadou Makhtar Ndiaga Diouf[1], Franck Lefèvre[1], Alain Hauchecorne[1], and Jean-Loup Bertaux[1]

[1]LATMOS, CNRS, Sorbonne Université, UVSQ Université Paris-Saclay, Paris, France

Key Points:

- Three-dimensional simulations of the $O_2(^1\Delta)$ dayglow at 1.27 μm are compared to satellite data
- The model and observations show that O_3 and $O_2(^1\Delta)$ near the stratopause and in the lower mesosphere are anti-correlated with temperature
- The $O_2(^1\Delta)$ brightness at 1.27 μm calculated with reanalyzed temperatures is on average $-4.2 \pm 2.8\%$ lower than the observations

Correspondence to:
M. M. N. Diouf,
mouhamadou.diouf@latmos.ipsl.fr

Citation:
Diouf, M. M. N., Lefèvre, F., Hauchecorne, A., & Bertaux, J.-L. (2024). Three-dimensional modeling of the $O_2(^1\Delta)$ dayglow: Dependence on ozone and temperatures. *Journal of Geophysical Research: Atmospheres*, *129*, e2023JD040159. https://doi.org/10.1029/2023JD040159

Received 6 OCT 2023
Accepted 18 MAR 2024

Abstract Future space missions dedicated to measuring CO_2 on a global scale can make advantageous use of the O_2 band at 1.27 μm to retrieve the air column. The 1.27 μm band is close to the CO_2 absorption bands at 1.6 and 2.0 μm, which allows a better transfer of the aerosol properties than with the usual O_2 band at 0.76 μm. However, the 1.27 μm band is polluted by the spontaneous dayglow of the excited state O_2 ($^1\Delta$), which must be removed from the observed signal. We investigate here our quantitative understanding of the $O_2(^1\Delta)$ dayglow with a chemistry-transport model. We show that the previously reported −13% deficit in $O_2(^1\Delta)$ dayglow calculated with the same model is essentially due a −20% to −30% ozone deficit between 45 and 60 km. We find that this ozone deficit is due to excessively high temperatures (+15 K) of the meteorological analyses used to drive the model in the mesosphere. The use of lower analyzed temperatures (ERA5), in better agreement with the observations, slows down the hydrogen-catalyzed and Chapman ozone loss cycles. This effect leads to an almost total elimination of the ozone and $O_2(^1\Delta)$ deficits in the lower mesosphere. Once integrated vertically to simulate a nadir measurement, the deficit in modeled $O_2(^1\Delta)$ brightness is reduced to $-4.2 \pm 2.8\%$. This illustrates the need for accurate mesospheric temperatures for a priori estimations of the $O_2(^1\Delta)$ brightness in algorithms using the 1.27 μm band.

Plain Language Summary Future space missions dedicated to measuring CO_2 in the atmosphere can make advantageous use of the O_2 absorption band at 1.27 μm. Indeed, the 1.27 μm band is close to the wavelengths where CO_2 absorbs the solar radiation, which allows more precise calculations. However, the 1.27 μm band is polluted by the spontaneous infrared emission of O_2 in its excited state called $O_2(^1\Delta)$, which occurs in the upper atmosphere and must be removed from the observed signal. We investigate here our understanding of the $O_2(^1\Delta)$ emission with a chemistry-transport model. When compared to observations, there is a −13% deficit in $O_2(^1\Delta)$ in our model. We find that this deficit is due to excessively high temperatures (+15 K) used in the calculations. The use of temperatures more in line with the observations slows down the ozone-destroying chemical cycles, which leads to an almost total elimination of the $O_2(^1\Delta)$ deficit. Once integrated vertically to simulate a satellite measurement, the deficit in modeled $O_2(^1\Delta)$ brightness is reduced to $-4.2 \pm 2.8\%$. This illustrates the need for accurate temperatures in the middle atmosphere for a reliable prediction of the $O_2(^1\Delta)$ emission occurring in the 1.27 μm band.

1. Introduction

In order to map, on a global scale, the sources and sinks of CO_2, the French national center for space studies (CNES) will launch in late 2025 the MicroCarb space mission (Pasternak et al., 2017). The mission builds on a high spectral resolution infrared grating spectrometer aboard a microsatellite and will be launched on a 10:30 hr descending node heliosynchronous orbit. Spaceborne measurement of the CO_2 mixing ratio usually relies on the determination of the CO_2/O_2 column ratio. Up to now, instruments dedicated to that objective, such as OCO-2 (Frankenberg et al., 2015) and GOSAT (Kuze et al., 2016), have retrieved the CO_2 and O_2 columns respectively from the CO_2 absorption bands at 1.6 and 2.0 μm, and the O_2 absorption band at 0.76 μm. However, the spectral distance between the so-called A band of O_2 at 0.76 μm and the CO_2 absorption band at 1.6 μm introduces significant uncertainties. Indeed, the spectral variations of the aerosol optical properties between 0.76 and 1.6 μm may lead to opticals paths that are substantially different for the photons in those two bands. Moreover, this O_2 A band is generally strong and largely saturated causing challenges on the radiative transfer modeling (Drouin et al., 2017).

The innovation in the MicroCarb mission is the addition of the O_2 absorption band centered at 1.27 μm, closer to the CO_2 bands. Absorption lines in this band are also weaker than those in the 0.76 μm band, improving the

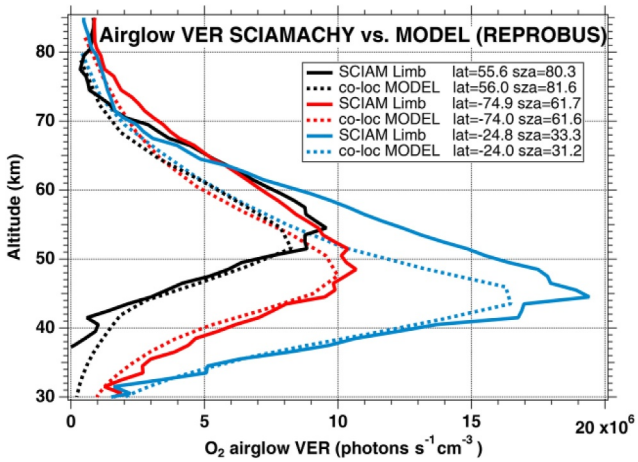

Figure 1. Example of the $O_2(^1\Delta)$ volume emission rate (photons cm^{-3} s^{-1}) observed by SCIAMACHY and calculated by the REPROBUS model for 3 January 2007. Three profiles are drawn at solar zenith angles (SZA) of about 30°, 60°, and 80°, indicated in the legend. The SCIAMACHY profiles are plotted as solid lines and the colocated REPROBUS profiles are plotted as dashed lines. From Bertaux et al. (2020).

accuracy of radiative transfer modeling. However, the band at 1.27 μm is polluted by the spontaneous emission of O_2 in its excited state O_2 ($^1\Delta$), which is produced essentially by the photodissociation of ozone (O_3) molecules (Mlynczak et al., 1993):

$$O_3 + h\nu \rightarrow O(^1D) + O_2(^1\Delta) \quad (1)$$

The dayglow at 1.27 μm occurs mainly at altitudes above 40 km, when the first excited state $O_2(^1\Delta)$ relaxes spontaneously to its ground state $O_2(^3\Sigma_g^-)$:

$$O_2(^1\Delta) \rightarrow O_2(^3\Sigma_g^-) + h\nu \ (\lambda = 1.27\mu m) \quad (2)$$

The $O_2(^1\Delta)$ dayglow at 1.27 μm is one of the most intense lines measured in the atmosphere of telluric planets. It has been observed from satellites instruments such as the Solar Mesosphere Explorer (SME) (Thomas et al., 1984), the Optical Spectrograph and InfraRed Imager System (OSIRIS) spectrometer onboard ODIN (Llewellyn et al., 2004), the SCIAMACHY spectrometer onboard ENVISAT (Bovensmann et al., 1999; Burrows et al., 1995; Zarboo et al., 2018), or SABER onboard TIMED (Mlynczak et al., 2007; Russell et al., 1999) etc. It has also been observed from aircraft (Noxon and Vallance Jones, 1962), from rockets (Evans et al., 1968; Jones & Welker, 1970), and from the ground (Sandor et al., 1997).

The contamination by the $O_2(^1\Delta)$ dayglow is the reason why, up to now, the band at 1.27 μm has not been used by CO_2 monitoring space missions. Recently, Bertaux et al. (2020) have found that the performance of MicroCarb allowed distinguishing the airglow from the absorption spectrum with great accuracy. Thus, it was decided to include the 1.27 μm band in the instrument design. To carry out the separation of the absorption and emission of O_2, MicroCarb will use a priori quantitative information on the $O_2(^1\Delta)$ dayglow calculated by the REPROBUS chemistry-transport model (Lefevre et al., 1994) driven by operational ECMWF analysis of wind and temperature. However, Bertaux et al. (2020) also found that the REPROBUS model consistently underestimated the vertically integrated $O_2(^1\Delta)$ emission by about 13% relative to the measurements of SCIAMACHY in nadir mode. When compared to the limb observations of SCIAMACHY, the discrepancy between the model and the observations is essentially located between 40 and 70 km (Figure 1). In this layer straddling the upper stratosphere and lower mesosphere, REPROBUS underestimates the $O_2(^1\Delta)$ dayglow by 10%–45%, the maximum deficit being found just above the stratopause around 57 km in the tropics. Bertaux et al. (2020) attributed this discrepancy to the ozone deficit noted in the model relative to the measurements of the GOMOS instrument onboard ENVISAT. This result is reminiscent of the early work of Sandor et al. (1997), who compared measurements of the $O_2(^1\Delta)$ airglow obtained with the National Radio Astronomy Observatory (NRAO) in January 1992 to a one-dimensional photochemical model (Siskind et al., 1995). They also found that their model underpredicted $O_2(^1\Delta)$ by an average of 17% (ranging from 3% to 33%) between 50 and 70 km. Sandor et al. (1997) pointed out that the underestimation of the $O_2(^1\Delta)$ airglow was consistent with the underestimation of the amount of ozone calculated by their model in the mesosphere.

The objective of this work is to investigate the deficit in the modeled $O_2(^1\Delta)$ dayglow diagnosed by Bertaux et al. (2020). As ozone photolysis is the main source of the $O_2(^1\Delta)$ dayglow, we first conduct a quantitative study of the ozone calculated by the model in the upper stratosphere and mesosphere, which is compared to satellite ozone observations. We then look at the impact of temperature on mesospheric ozone, and reanalyze the historical problem of the ozone deficit in the models at 40–45 km (Butler, 1978; Eluszkiewicz & Allen, 1993). Finally, we compare the $O_2(^1\Delta)$ dayglow calculated with an optimized simulation to observations by the SABER instrument.

2. Model Description

2.1. The REPROBUS Chemistry-Transport Model

Here we use the latest version of the REPROBUS three-dimensional Chemistry-Transport Model (CTM). This model was initially described in Lefevre et al. (1994, 1998) but has been profoundly reworked since these early

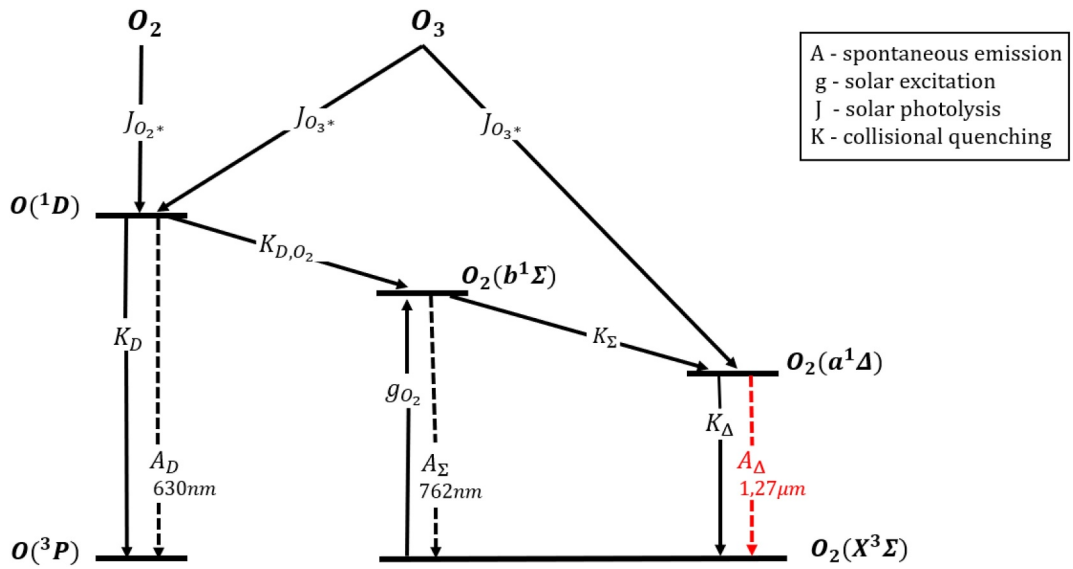

Figure 2. Illustration of the mechanisms resulting in the O_2 ($^1\Delta$) dayglow at 1.27 μm (in red) implemented in the model. Adapted from Mlynczak et al. (1993).

studies. In particular, REPROBUS has adopted the adaptive semi-implicit scheme (ASIS) developed by Cariolle et al. (2017) to solve the ordinary differential equation systems associated with the time evolution of the species concentrations. This solver strictly conserves mass and does not require a priori hypothesis on the lifetime of chemical tracers or species lumping. The description of stratospheric and mesospheric chemistry is comprehensive. It takes into account the densities of 58 species, by means of 125 reactions (gas-phase and heterogeneous) and 63 photodissociations. As in Lefèvre et al. (1998), photodissociation frequencies are precalculated by the TUV radiative model (Madronich & Flocke, 1998), which are then stored in a four-dimensional lookup table expressed as a function of altitude, SZA, ozone column and albedo. The chemical rate constants and absorption cross-sections are in general those recommended by the latest JPL compilation (Burkholder et al., 2019). Regarding transport, all species are advected separately using the semi-Lagrangian scheme of Williamson and Rasch (1989).

The temperatures and winds that drive the photochemistry and transport in the model are taken from the 3-hourly ECMWF analysis. In the configuration used here, the horizontal resolution of REPROBUS is 2° latitude x 2° longitude and its vertical domain extends from the ground to 0.01 hPa (about 80 km). The vertical levels are discretized in the same way as the analysis used to drive the model: for the year 2007 considered here, REPROBUS has 91 hybrid pressure levels as the ECMWF analysis that was operational for that year. This leads to a vertical resolution of about 0.5 km in the lower stratosphere, 2 km in the upper stratosphere, and 3 km in the mesosphere. When using the ECMWF ERA5 reanalysis (Herbach et al., 2020) for the same year, the model has 137 pressure levels and the vertical resolution is respectively increased to about 0.3, 1, and 2.5 km. The vertical coverage of the ERA5 analyses is identical to the operational version and extends from the surface to 0.01 hPa.

2.2. Implementation of the $O_2(^1\Delta)$ Photochemistry

The comprehensive chain of production and loss mechanisms of $O_2(^1\Delta)$ leading to the airglow at 1.27 μm has been implemented in REPROBUS (Figure 2). Table 1 lists the photolytic and gas phase reactions linked to the $O_2(^1\Delta)$ airglow in the model. All species are transported individually and the $O_2(^1\Delta)$ airglow is calculated on-line by REPROBUS. This is an improvement over the version of REPROBUS used in Bertaux et al. (2020), for which $O_2(^1\Delta)$ was assumed to be in photochemical equilibrium and the airglow was calculated off-line from the model outputs.

When ozone photodissociates at wavelengths below 310 nm, it splits into a molecule of oxygen in its first excited state $O_2(^1\Delta)$ and an oxygen atom in its first excited state $O(^1D)$ with a quantum yield of about 0.9 (photolysis J_{O3*} in Table 1). Ozone photolysis accounts for around 80% of the total production of $O_2(^1\Delta)$ and is therefore the main

Table 1
Photolytic and Gas Phase Reactions Involved in $O_2(^1\Delta)$ Production and Loss in the REPROBUS Model

	Reactions	Rate	References
$J_{O_2^*}$	$O_2 + h\nu \rightarrow O(^1D) + O$		Ogawa and Ogawa (1975); Lewis et al. (1983); Gibson et al. (1983)
$J_{O_3^*}$	$O_3 + h\nu \rightarrow O(^1D) + O_2(^1\Delta)$		Burkholder et al. (2019)
g_{O_2}	$O_2(^3\Sigma_g^-) + h\nu\ (\lambda = 762\ nm) \rightarrow O_2(b^1\Sigma)$		Winsz (2005)
A_Δ	$O_2(^1\Delta) \rightarrow O_2(^3\Sigma_g^-) + h\nu\ \ (\lambda = 1.27\ m)$	2.237×10^{-4}	Lafferty et al. (1998)
A_D	$O(^1D) \rightarrow O(^3P) + h\nu\ \ (\lambda = 630\ nm)$	7.46×10^{-3}	Baluja and Zeippen (1988)
A_Σ	$O_2(b^1\Sigma) \rightarrow O_2(^3\Sigma_g^-) + h\nu\ \ (\lambda = 762\ nm)$	0.0758	Mlynczak and Salomon (1993)
$K_{\Sigma,O}$	$O_2(b^1\Sigma) + O(^3P) \rightarrow O_2(^1\Delta) + O(^3P)$	8×10^{-14}	Burkholder et al. (2019)
K_{Σ,O_2}	$O_2(b^1\Sigma) + O_2 \rightarrow O_2(^1\Delta) + O_2(^3\Sigma_g^-)$	$3.9\ 10^{-17}$	Burkholder et al. (2019)
K_{Σ,O_3}	$O_2(b^1\Sigma) + O_3 \rightarrow O_2(^1\Delta) + O_3$	$3.5 \times 10^{-11} \times \exp(-135/T) \times 0.3$	Burkholder et al. (2019)
K_{Σ,N_2}	$O_2(b^1\Sigma) + N_2 \rightarrow O_2(^1\Delta) + N_2$	$1.8 \times 10^{-15} \times \exp(45/T)$	Burkholder et al. (2019)
K_{Σ,CO_2}	$O_2(b^1\Sigma) + CO_2 \rightarrow O_2(^1\Delta) + CO_2$	4.2×10^{-13}	Burkholder et al. (2019)
K_{D,O_2}	$O(^1D) + O_2 \rightarrow O_2(b^1\Sigma) + O(^3P)$	$3.3 \times 10^{-13} \times \exp(55/T)$	Burkholder et al. (2019)
K_{D,N_2}	$O(^1D) + N_2 \rightarrow O(^3P) + N_2$	$2.15 \times 10^{-11} \times \exp(110/T)$	Burkholder et al. (2019)
K_{Δ,O_2}	$O_2(^1\Delta) + O_2 \rightarrow O_2 + O_2$	$3.0 \times 10^{-18} \times \exp(-200/T)$	Atkinson et al. (2005)

Note: J are photolysis frequencies (s^{-1}) and g is the solar excitation rate (s^{-1}). Processes noted A are spontaneous transition probabilities (s^{-1}) and K are collisional reaction rates ($molecules^{-1}.\ cm^3.\ s^{-1}$). T is the temperature (K).

original source for the airglow at 1.27 μm. A minor but non-negligible contribution (about 20%) to the production of $O_2(^1\Delta)$ comes from the excited oxygen $O(^1D)$ produced by O_3 photolysis and the energy cascade that follows. Indeed, $O(^1D)$ relaxes toward its ground state $O(^3P)$ in the mesosphere and stratosphere either radiatively, by emitting a photon at 630 nm, or by collisional quenching with a molecule of N_2 or O_2. Collisional quenching with O_2 produces the second excited state $O_2(b^1\Sigma)$. The $O_2(b^1\Sigma)$ state can also be produced by solar excitation, when O_2 absorbs a solar photon in the A band at 762 nm (g_{O2} in Table 1). The contribution of this process to the production of $O_2(^1\Delta)$ becomes important only above 60 km. Finally, the collisional quenching of $O_2(b^1\Sigma)$ with O, O_2, O_3, N_2, and CO_2 leads to the lower energy state $O_2(^1\Delta)$. As shown by Mlynczak et al. (1993), $O(^1D)$ atoms can also be produced in the thermosphere and upper mesosphere by the O_2 photolysis in the Schumann-Runge continuum and in the Lyman alpha line (J_{O2*} in Table 1). This process not included in the version of the model used by Bertaux et al. (2020) has been added to the current version of REPROBUS.

Once produced in its state $O_2(^1\Delta)$, molecular oxygen transmits its energy either through radiative relaxation or by quenching with surrounding molecules. Radiative relaxation operates by emission of a photon at 1.27 μm. This transition takes place with a fairly long time constant. The current consensus for the radiative lifetime of $O_2(^1\Delta)$ is $1/A_\Delta = 75$ mn (Lafferty et al., 1998; Mlynczak et al., 2007). At altitudes below 75 km, collisional quenching dominates over radiative relaxation. We have adopted the value of the quenching rate of the $O_2(^1\Delta)$ recommended by the International Union of Pure and Applied Chemistry panel (IUPAC, Atkinson et al., 2005) rather than by the JPL panel (Burkholder et al., 2019). The IUPAC recommended value is slightly lower than that of JPL (−10%), which allows a better agreement with observational data (Bertaux et al., 2020; Wiensz, 2005).

3. Observational Data

3.1. Temperature, O_3, HO_x: MLS on Board AURA

The results of our simulations will be compared to measurements of temperature, ozone, and HO_x radicals (defined as the sum of OH and HO_2) performed from the Microwave Limb Sounder (MLS). MLS is a microwave spectrometer and one of four instruments on the NASA AURA satellite, launched in 2004 (Waters et al., 2006). Located on the A-train group of Earth observing satellites, AURA is in a quasi-polar sun-synchronous orbit (ascending node of 13:45 LT) at an altitude of 705 km. MLS measures the millimeter and submillimeter thermal emission in five spectral regions from 115 GHz to 2.5 THz in order to retrieve profiles of temperature and concentrations of over 15 atmospheric trace species. Scanning the Earth's atmospheric limb every 24.7s, MLS

provides 240 scans per orbit and 3,500 per day with a footprint of ∼6 km across-track and ∼ 150 km along-track with a spatial coverage between 82°N and 82°S. We have used in this study version 5 of the MLS products (Livesey et al., 2020).

MLS retrieves temperature profiles primarily from bands near O_2 spectral lines at 239 GHz for the troposphere, and at 118 GHz for the stratosphere (Livesey et al., 2020). The temperature is retrieved on 47 pressure levels with a vertical resolution of 3–4 km from 261 to 10 hPa, 7–8 km at 1–0.1 hPa, and 11 km at 0.01 hPa. The precision of MLS single temperature profile ranges from 0.5 K in the lower stratosphere to ∼3.4 K in the mesosphere.

From radiance measurements measured near 240 GHz, MLS retrieves ozone profiles on 55 pressure levels between 261 and 0.001 hPa with a vertical resolution estimated to be 2.5–5.5 km from the upper troposphere to the middle mesosphere. The estimated precision for a single profile (i.e., non-averaged) is about 2%–3% between 16 and 50 km and gradually drops to 20%–50% between 50 and 70 km. Jiang et al. (2007), Livesey et al. (2008) and Froidevaux et al. (2008) have described the detailed validation of the MLS V2.2 products and their comparison with other data sets. The results of those validations are generally applicable to the version 5 stratospheric O_3 data.

Hydroxyl radical (OH) is measured at 2.5 THz. MLS provides the OH product on 49 pressure levels, and it is recommended, for scientific purposes, to use specifically those in the pressure range from 32 to 0.0032 hPa. The vertical resolution for the OH MLS product is 2.5 km between 32 and 0.01 hPa. The precision on an individual profile is estimated to be 4.7×10^6 cm^{-3} around 10 hPa and 3.6×10^6 cm^{-3} around 0.1 hPa. The relative precision is better than 10% for the OH zonal average within a 10° latitude bin with one day of data (∼100 samples) over 21–0.01 hPa. The HO_2 measurements are made from two HO_2 lines centered at 649.72 and 660.50 GHz. The smallness of the HO_2 signal translates to a retrieved product useable only between 10 and 0.046 hPa. The vertical resolution of HO_2 MLS product varies from 4 km at 10 hPa to 5 km at 1 hPa and 7 km at 0.1 hPa. The precision for a single profile varies from 56×10^6 cm^{-3} at 10 hPa to 4×10^6 cm^{-3} at 0.046 hPa. Since negligible HO_2 is expected at night, the day-night HO_2 difference is necessary to reduce systematic errors to an acceptable level (Livesey et al., 2020). The OH and HO_2 measurement technique, instrument calibration, and validation studies are described in Pickett et al. (2006, 2008) and Wang et al. (2013).

3.2. O_2 ($^1\Delta$) Airglow: SABER Onboard TIMED

Regarding the $O_2(^1\Delta)$ airglow, we will use as an observational reference the measurements by the Sounding of the Atmosphere using the Broadband Emission Radiometry (SABER) instrument (Mlynczak, 1997; Mlynczak & Russell, 1995). SABER is a 10 channel-scanning radiometer onboard the NASA Thermosphere Ionosphere Mesosphere Energetics and Dynamics (TIMED) launched in 2001. TIMED was placed into a non-sun synchronous orbit, at an altitude of 625 km, with an orbital inclination of 74.1° and a mean orbit period of 1.6 hr. The equator crossing shifts by about 12 mn per day.

One of the channels of SABER is centered at 1.27 μm, with a nominal transmission of 5% from 1.298 to 1.254 μm, which allows measuring the $O_2(^1\Delta)$ airglow. The noise equivalent radiance in the SABER $O_2(^1\Delta)$ channel is 2.4×10^{-10} W cm^{-2} sr^{-1} and the signal-to-noise ratio exceeds 1000 below 90 km tangent altitude (Mlynczak et al., 2007). The main product derived from this channel, generally used to recover diurnal ozone, is the volume emission rate (VER, in photons. cm^{-3}. s^{-1}) of $O_2(^1\Delta)$, which is provided by SABER between 40 and 105 km. With 53 s to sweep a limb radiation profile, SABER provides approximately 96 vertical profiles per orbit. This represents over 1400 profiles per day with a sampling rate that translates to approximately 0.38 km spacing between samples for each profile. Its spatial coverage alternates approximately every 2 months from 83°S-52°N to 52°S-83°N and it takes about 60 days to complete a full 24-hr coverage in local time (Dakermanji et al., 1997). We use here the latest publicly available version 2.0 of SABER data.

4. Model Results

4.1. Ozone (O_3)

Ozone photolysis being the main driver of the $O_2(^1\Delta)$ airglow, we first compare the ozone calculated by REPROBUS to contemporaneous observations of MLS. For the first simulation considered here (hereafter named "nominal simulation"), REPROBUS is driven by the ECMWF operational analysis and is integrated from 1 January 2007–31 December 2007.

Figure 3 (top and middle) shows the zonally averaged O_3 distribution observed by MLS and calculated by REPROBUS for four representative months (equinoxes and solstices) of the year 2007. Overall, the model represents very well the morphology of the observed zonally averaged distribution of O_3, as well as its seasonal variations. The quantitative agreement between MLS and REPROBUS can be examined in more detail in Figure 3 (bottom). It reveals that the O_3 is generally underestimated in REPROBUS in the altitude region between 30 and 70 km. In the upper stratosphere (30–50 km), the modeled O_3 is 5%–15% lower than MLS. A greater difference is found in the mesosphere (50–70 km), where the underprediction of O_3 in REPROBUS reaches about −30% at 60 km relative to the observations. In the lower stratosphere (20–30 km), the modeled O_3 is on the contrary 5%–10% higher than MLS.

The vertical domain and the amplitude of the O_3 underestimation in REPROBUS are remarkably consistent with the underestimation of the $O_2(^1\Delta)$ dayglow in the model as reported by Bertaux et al. (2020) and shown in Figure 1. As the $O_2(^1\Delta)$ dayglow at a given altitude is proportional to the amount of ozone, it is clear that the ozone deficit noted in REPROBUS is a major cause of the $O_2(^1\Delta)$ dayglow deficit in the model. In the following, we look at the possible causes of this lack of modeled ozone in the upper stratosphere and mesosphere.

4.2. Hydrogen Radicals (HO_x)

The ozone deficit problem is not just particular to the REPROBUS model. Historically, models have systematically underpredicted the concentration of ozone when compared to various observations at altitudes between 35 and 80 km (e.g., Butler, 1978; Eluszkiewicz & Allen, 1993; Frederick et al., 1978; Siskind et al., 2013; Solomon et al., 1983). The magnitude of the deficit was reported in the mid 1980s to be about 30%–40% in the upper stratosphere (Froidevaux et al., 1985). In the mesosphere, the ozone deficit reached a factor of two, which was attributed to a too high efficiency of the catalytic cycle of HO_x, the family of hydrogen radicals (OH and HO_2) that dominates mesospheric ozone loss (Rusch & Eckman, 1985).

Later studies showed an ozone deficit reduced to 25%–30% in the models, thanks to improvements in reaction rates parameters, better estimations of total reactive chlorine levels, and revised solar flux data (McElroy & Salawitch, 1989; Natarajan & Callis, 1989; Siskind et al., 1998). These improvements have tended to decrease the calculated HO_x. Despite this, in the late 1990s, overpredictions of OH by 25%–35% were still noted in the mesosphere when comparing model results to MAHRSI data (Conway et al., 1996, 2000; Summers et al., 1997). In parallel, a consistent deficit was observed in modeled HO_2, of the order of 25% in the stratosphere (Jucks et al., 1998) and between 23% and 47% in the mesosphere (Sandor & Clancy, 1998). A tantalizing solution to this problem is to reduce the rate of the reaction between HO_2 and O, which results in less OH, more HO_2, and slower odd oxygen removal. By reducing the rate of this reaction by 40%–50%, discrepancies between models and observations can be solved in the mesosphere (Clancy et al., 1994; Conway et al., 2000; Sandor & Clancy, 1998; Summers et al., 1997). However, this change worsens the model predictions of OH in the stratosphere (Jucks et al., 1998).

More recently, independent studies using the MLS (Pickett et al., 2008) and SHIMMER instruments (Englert et al., 2008) found a good agreement between the observed and modeled OH in the middle atmosphere. To explain this contradictory result with previous studies, Englert et al. (2010) argued that MAHRSI data may have unrecognized calibration issues resulting in lower OH abundances and concluded that models using the standard chemistry did not overpredict mesosphere OH. Canty et al. (2006) and Siskind et al. (2013) came to similar conclusions. Both studies found no evidence of a systematic model overprediction of mesospheric OH and argued that the model ozone deficit was unlikely to be due to a mischaracterization of mesospheric HO_x.

To reassess this problem with a model using the most recent recommended reaction rates for the HO_x chemistry, we have compared the distribution of HO_x (OH + HO_2) calculated by REPROBUS with that measured by MLS. Figure 4 shows the relative difference between the observed and calculated HO_x mixing ratio for the same 4 months of 2007 already considered for ozone, and concerns only daytime HO_x (SZA less than 75°). The comparison reveals a rather good agreement throughout the middle atmosphere. For the four selected months REPROBUS generally underestimates HO_x, but the difference is less than 10% in the stratosphere and lower mesosphere up to 60 km. A greater difference of about 30%–40% can be seen near the top of the model at 70 km. The underestimation of the HO_x calculated by REPROBUS may have multiple causes, the most obvious ones being inaccurate reaction rates or temperatures. However, these results do not reveal a major flaw in our quantitative understanding of the HO_x chemistry in the middle atmosphere. It can be argued that the current kinetic

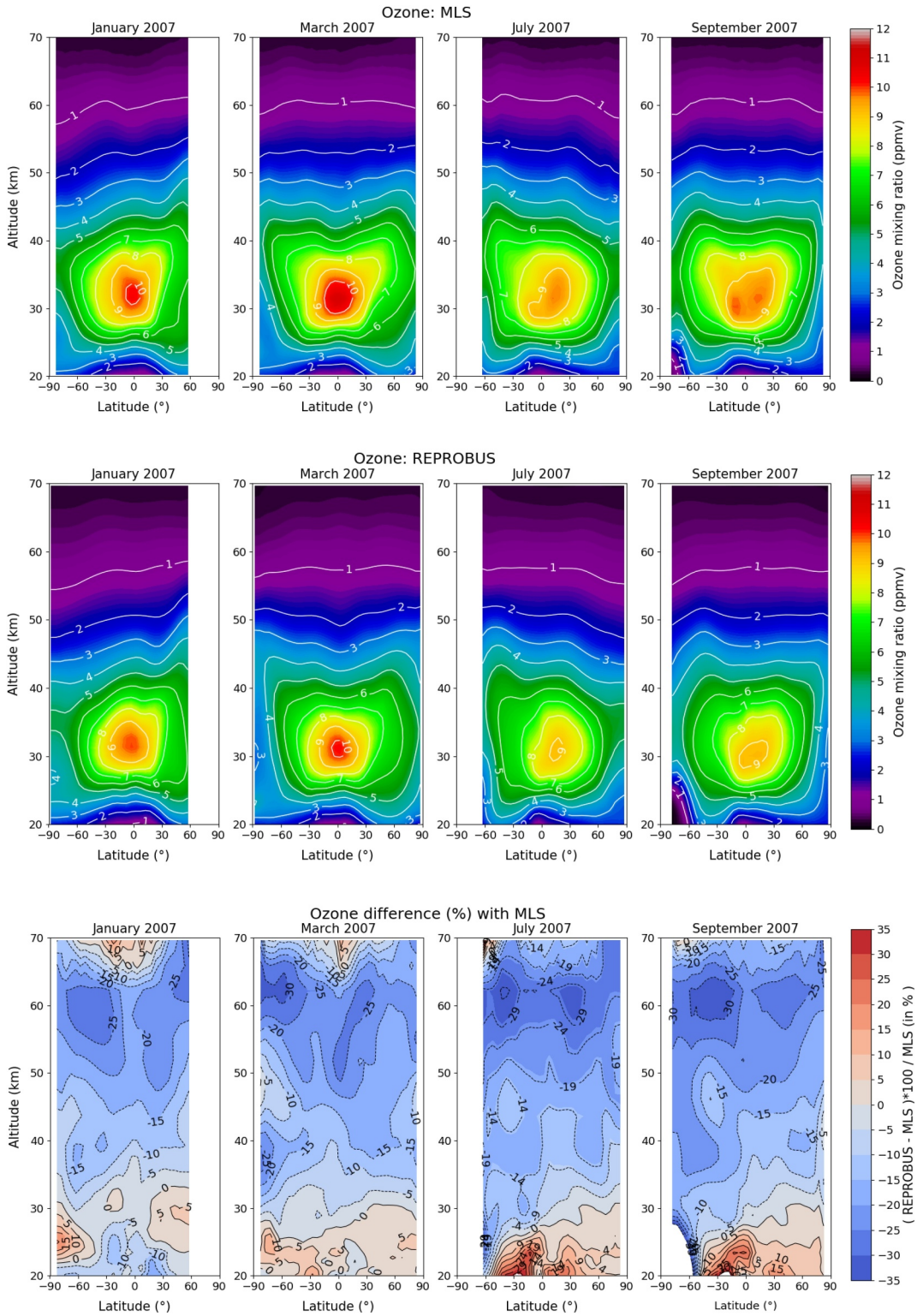

Figure 3. Top: Zonally averaged O_3 mixing ratio (ppmv) observed by MLS. Middle: Zonally averaged O_3 mixing ratio (ppmv) calculated by REPROBUS with the ECMWF operational analysis. Bottom: Difference (%) between REPROBUS and MLS. The difference is calculated as (REPROBUS - MLS)/MLS x100. From left to right: January, March, July and September 2007 during daytime (SZA <85°).

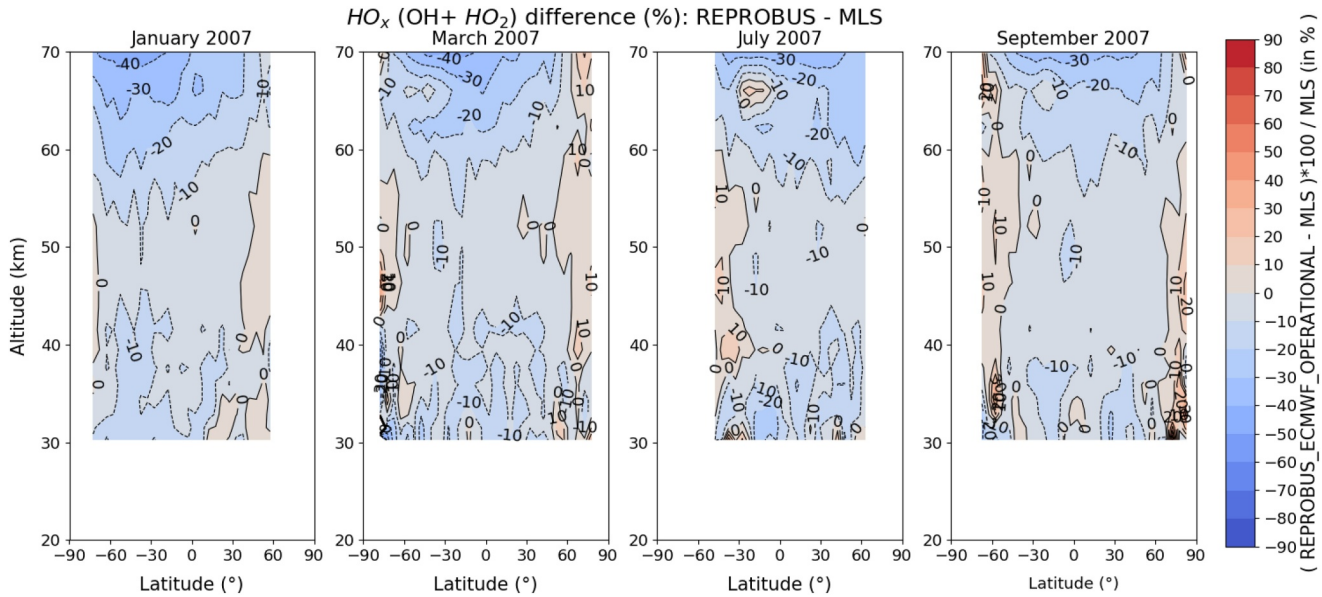

Figure 4. Zonally averaged difference (%) between the HO_x mixing ratio calculated by REPROBUS and observed by MLS. HO_x is defined as the sum OH + HO_2, and the difference is calculated as (REPROBUS-MLS)/MLS × 100. From left to right: January, March, July and September 2007 during daytime (SZA < 75°).

data set enables reasonable reproduction of the HO_x, even if imperfections remain in the upper mesosphere. The key point here is that the large underestimation of O_3 in REPROBUS around 60 km does not coincide with an overestimation of HO_x radicals. On the contrary, the HO_x mixing ratio calculated by the model in this altitude range is slightly underestimated (−10%) relative to observations. Similarly to Siskind et al. (2013), we conclude that a poor representation of the HO_x (such as a large overestimation) is not the reason for the lack of ozone in our model, which must be sought elsewhere.

4.3. Impact of Temperature

We now turn to the sensitivity of our results to temperature. Indeed, in their extensive study of the ozone deficit problem, Khosravi et al. (1998) identified that the lack of ozone in their simulations could be significantly reduced by using temperature data in better agreement with the observations. However, their study was limited to the upper stratosphere (37–50 km) and did not investigate the mesosphere.

In the nominal simulation, the temperatures used to drive the chemistry of REPROBUS are forced by the version of the ECMWF analysis that was operational in 2007 (Figure 5, top). These analysis were produced by the cycles Cy31r2, Cy32r2, and Cy32r3 of the ECMWF Integrated Forecasting System (IFS). When compared to the MLS measurements of temperature (Schwartz et al., 2008), the zonally averaged ECMWF temperatures for the four selected months of 2007 show a good agreement in the stratosphere up to about 50 km (Figure 5, bottom). However, above that altitude, the ECMWF operational analysis are significantly higher than the MLS temperatures with a warm bias of about 10–15 K in the mesosphere. This result is fairly in line with the validation study of Schwartz et al. (2008), who found that the ECMWF operational analysis in the mesosphere were warmer than the MLS temperatures by close to 10 K in the 50°S-50°N latitude band.

In the same spirit as Khosravi et al. (1998), we have investigated whether the warm bias of the temperatures used by REPROBUS in the mesosphere could have a significant effect on the ozone deficit in the model. For that purpose, we carried out a second REPROBUS simulation of the year 2007, for which the ECMWF operational analysis were replaced by the ECMWF ERA5 reanalysis to drive the model temperatures and winds. ERA5 is based on the IFS Cy41r2 cycle that was operational in 2016 (Herbach et al., 2020). It thus benefits from a decade of developments in model physics, core dynamics and data assimilation compared to the IFS version of 2007. In particular, ERA5 includes the parametrization for the non-orographic gravity wave drag and a more realistic greenhouse gas climatology, both introduced in IFS in 2009, which lead to substantial improvements in the temperature structure of the upper stratosphere and mesosphere (Bechtold et al., 2009).

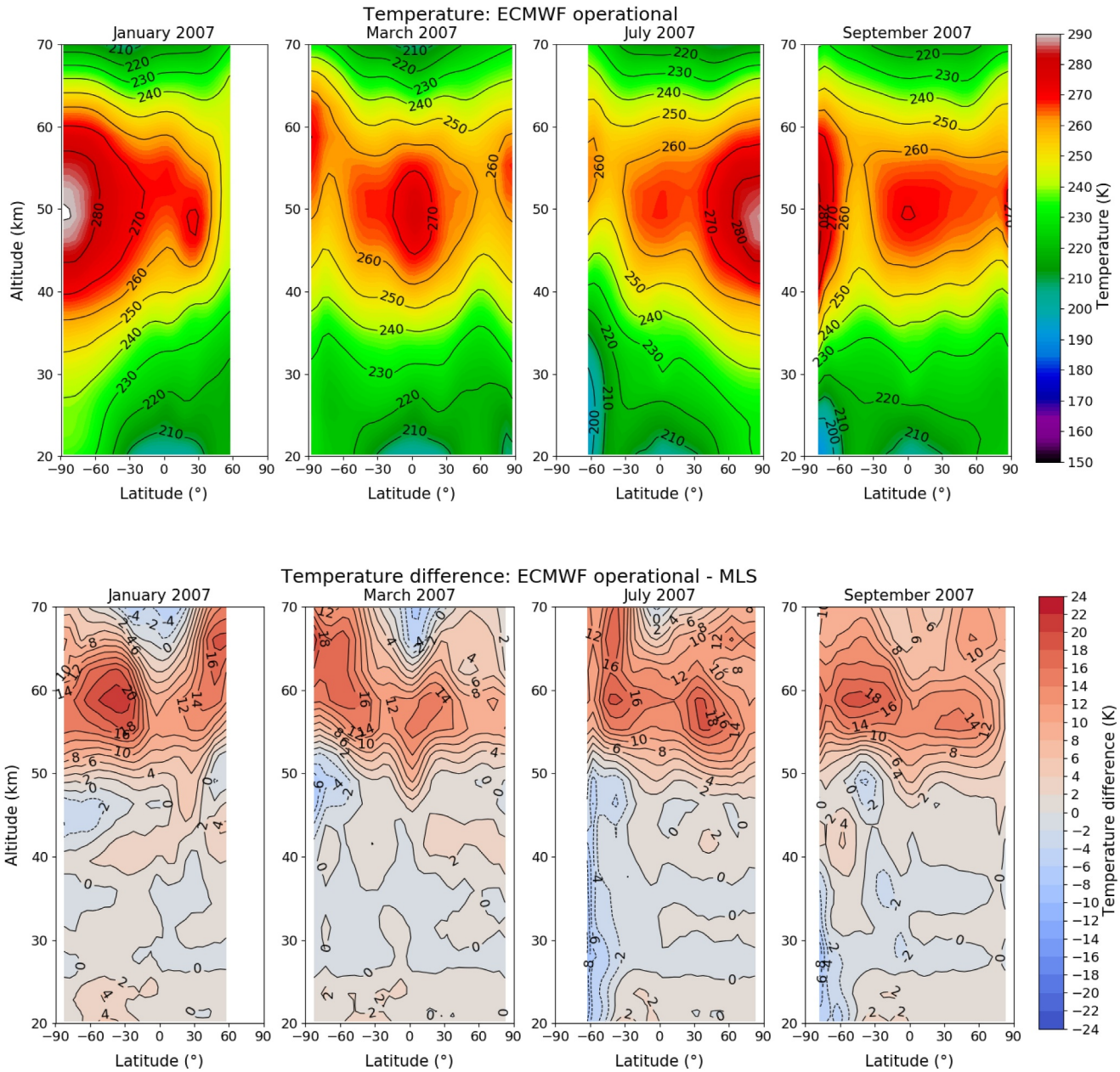

Figure 5. Top: Zonally averaged temperature (K) of ECMWF operational analysis. Bottom: difference (K) with MLS. From left to right: January, March, July and September 2007 during daytime (SZA < 85°).

Figure 6 (top) presents the zonally averaged ERA5 temperatures for the four months considered in 2007, and the difference with MLS temperatures. Below 45 km, the ERA5 temperatures are similar to the operational analysis and the agreement with MLS remains generally better than 2 K in monthly average. In contrast, the ERA5 temperatures show a pronounced cooling with respect to the operational analysis at the stratopause and in the mesosphere. This effect is largely due to the improvements brought to the physics of the IFS model in 2009, as documented by Bechtold et al. (2009). Consequently, the warm bias observed in the mesosphere with the operational analysis is almost completely resorbed with ERA5 (Figure 6, bottom). On the contrary, we find at low-to-mid latitudes and 60 km a moderate cold bias of around 3 K in yearly average compared with MLS temperatures. We note that the cold bias is more pronounced at the summer poles, which could result from a too strong overturning circulation in the reanalysis. A cold bias in ERA5 reanalysis was also noted in the mesosphere by several studies that made comparisons with ground-based lidar observations (Ehard et al., 2017; Marlton

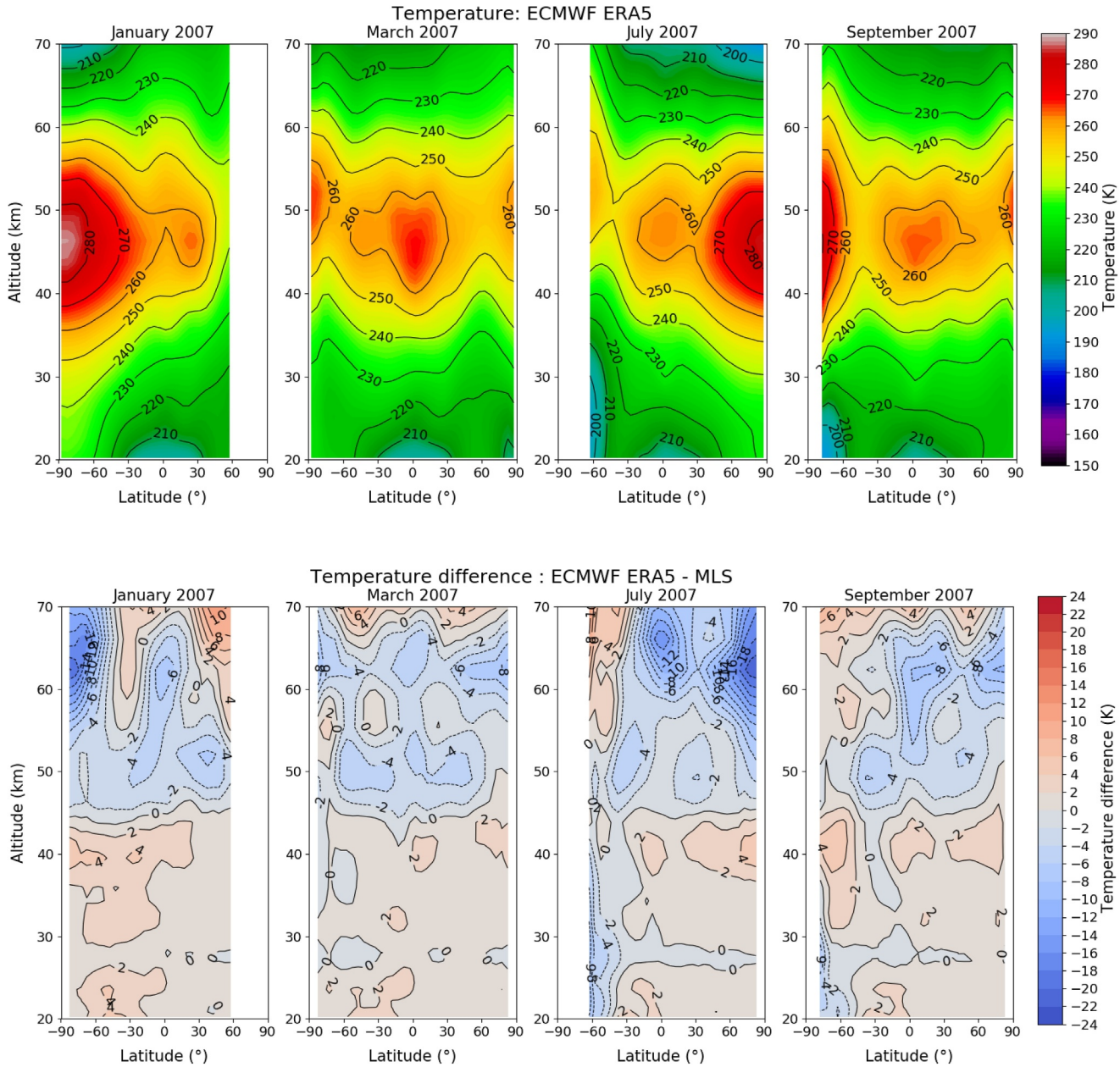

Figure 6. Top: Zonally averaged temperature (K) of ECMWF ERA5 reanalysis. Bottom: difference (K) with MLS. From left to right: January, March, July and September 2007 during daytime (SZA < 85°).

et al., 2021). Nevertheless, in absolute value, the agreement with MLS temperatures in the upper atmosphere is much improved with ERA5, and we can examine the ozone sensitivity to temperature when REPROBUS is forced by these reanalysis.

The zonally averaged O_3 mixing ratio calculated from the ERA5 reanalyses and the relative difference with MLS O_3 are shown respectively in Figure 7. Up to 45 km, the O_3 calculated with ERA5 shows little difference with that obtained with the operational analysis in Figure 3. A deficit of about 15% compared to MLS persists around 40 km altitude. This result is expected since the ERA5 temperatures do not show significant differences with the operational analysis in this altitude range. In contrast, there is a significant increase in O_3 with ERA5 at the stratopause and in the mesosphere. As a result, the average O_3 bias of REPROBUS relative to MLS decreases

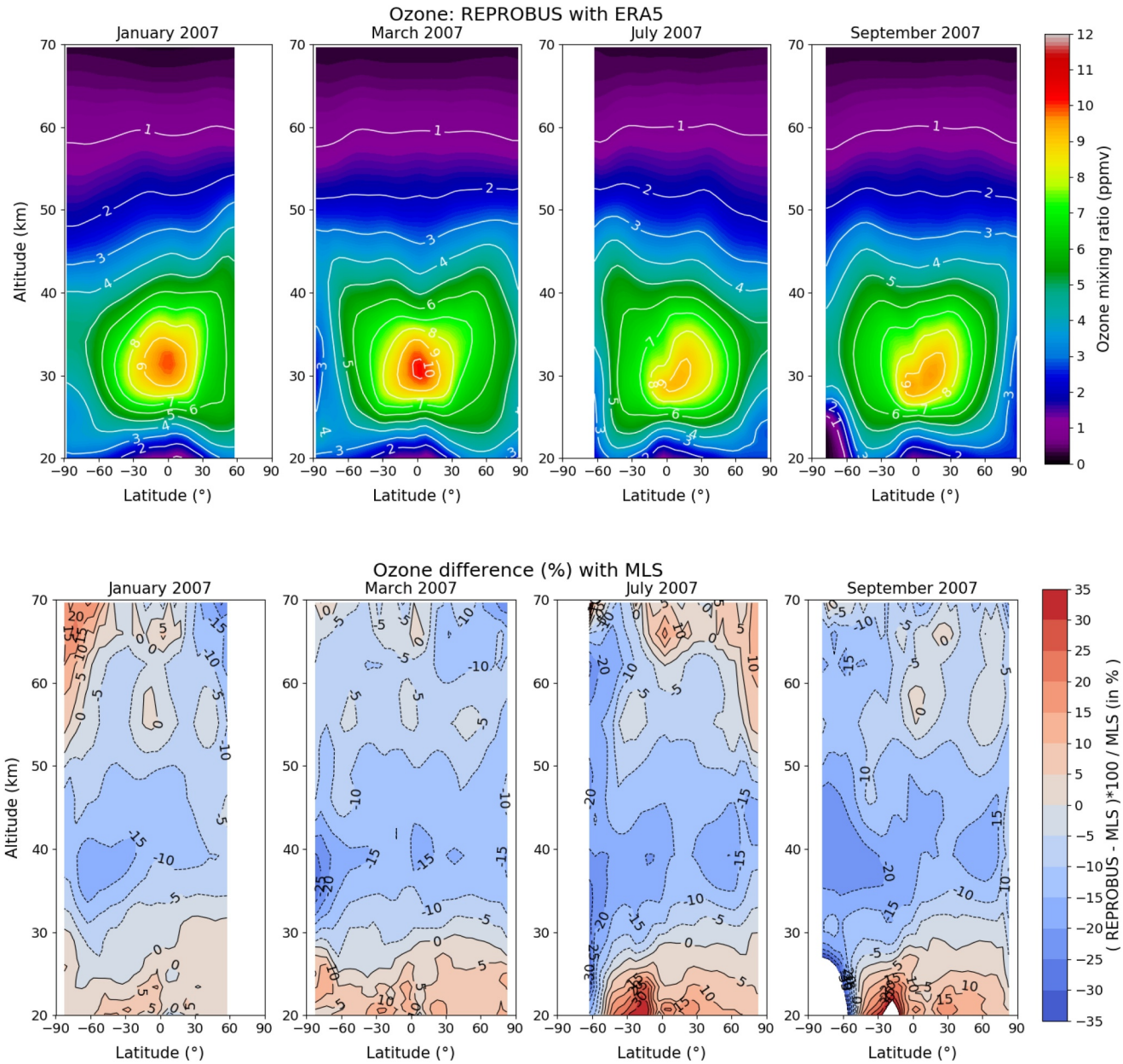

Figure 7. Zonally averaged O_3 mixing ratio (ppmv) calculated by REPROBUS with the ECMWF ERA5 reanalysis. Bottom: difference (%) with MLS. The difference is calculated as (REPROBUS - MLS)/MLS × 100. From left to right: January, March, July and September 2007 during daytime (SZA < 85°).

from about −25% to −5% in this altitude region. The bias even becomes positive at the summer poles, which is consistent with the too strong overturning circulation deduced from the cold bias in temperature in Figure 6.

These results show that, all other things being equal, temperature plays a major role in the amount of ozone present in the mesosphere. The fact that mesospheric ozone increases with decreasing temperature is evident when we adopt the ERA5 reanalyses in our simulations. This relationship can be further illustrated by the correlation plot between O_3 and temperature at 50 and 60 km, for both MLS and REPROBUS (Figure 8) in March. The data are restricted to the daytime period to avoid the effects of diurnal variations in ozone, which are by their nature independent of temperature. The results confirm that, at both levels, O_3 is anti-correlated with temperature during the day. REPROBUS reproduces relatively well the slope of the O_3-temperature relationship observed by MLS. At the stratopause (50 km), the model tends to underestimate ozone compared with MLS, as suggested by

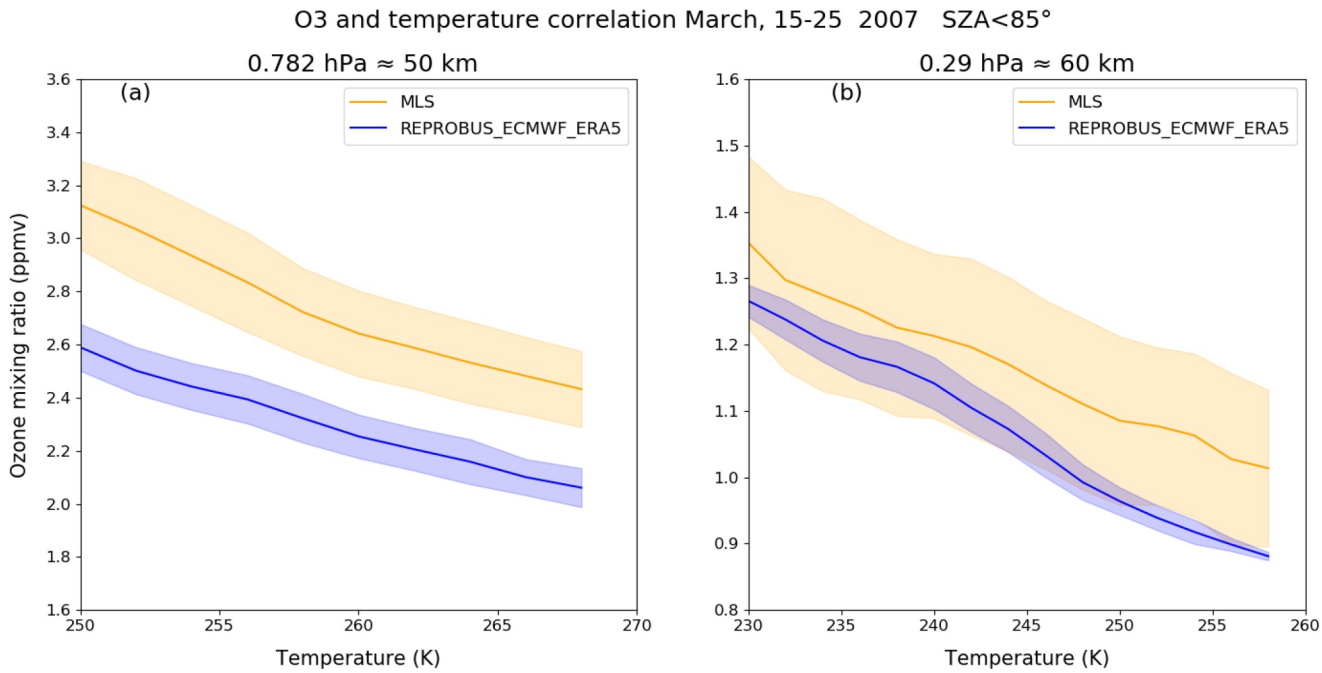

Figure 8. Relationship between ozone and temperature as observed by MLS (orange) and calculated by REPROBUS with the ERA5 reanalysis (blue). The curves show the average over the period 15–25 March 2017 for all points with SZA less than 85°. The shaded areas represent the 1-sigma standard deviation. (a) 0.782 hPa, about 50 km. (b) 0.29 hPa, about 60 km.

the zonal mean in Figure 7. The model results are in better agreement with MLS at 60 km, particularly at low temperatures, even though a moderate low O_3 bias is still visible.

To identify the causes of the inverse temperature dependance of ozone at the stratopause and in the mesosphere, we carried out an analysis similar to that of Jonsson et al. (2004), who studied the photochemical variation of ozone in the context of a doubled-CO_2 cooling in the middle atmosphere. Adopting their method, we linearized the ozone steady-state equation around the ozone steady-state of the REPROBUS reference experiment. Applying differentials to that equation allows us to quantify the relative contribution to the overall ozone change from the various parameters controlling the ozone budget. For the sake of simplicity, Figure 9 shows the result of this analysis for a single point at 10°N on 16 March 2007. On the left, Figure 9a compares the temperature profiles provided by the operational analysis and the ERA5 reanalysis. The cooler mesosphere is evident in ERA5, with temperatures around 20 K lower than the operational analysis in the 55–60 km range. On the right, Figure 9b shows the relative difference between the ozone profiles calculated with the operational analysis and with ERA5 respectively. The overall O_3 increase of up to 30% in the lower mesosphere obtained with the REPROBUS 3D simulations is rather well reproduced with the linearized equation of Jonsson et al. (2004), denoted here P- L. The term P represents the contribution to the overall ozone change from changes in the odd oxygen production rate. This term shows very little variation when the ERA5 temperatures are adopted in place of the operational analyses. The loss terms L_1, L_2, L_3, and L_4 represent respectively the contributions from changes in the Chapman (O_x), NO_x, ClO_x and HO_x odd oxygen loss cycles. It can be seen that the increase in O_3 is essentially due to a reduction in the efficiency of the HO_x cycles. The slower HO_x odd oxygen loss rate calculated with the cooler ERA5 temperatures explains more than 80% of the O_3 increase above 55 km. This lesser destruction of odd oxygen by HO_x is not due to a slowing down of the reaction rates coefficients k_1 of $HO_2 + O \rightarrow OH + O_2$ and k_2 of $OH + O \rightarrow H + O_2$. On the contrary, k_1 and k_2 show a slight acceleration (3%–5%) when the temperature decreases by 20 K. In agreement with Jonsson et al. (2004), we find that the major factor behind the O_3 increase is the strong increase in the rate coefficient k_3 of $O + O_2 + M \rightarrow O_3 + M$ (+30% for a cooling of 20 K), leading to a shift in odd oxygen partitioning. Increasing k_3 reduces the abundance of atomic oxygen. As the loss of odd oxygen by HO_x is proportional to the number density of atomic oxygen, increasing k_3 leads to a slower loss of odd oxygen by HO_x. Below 55 km, the temperature dependence of the Chapman loss reaction ($O + O_3 \rightarrow O_2 + O_2$) becomes a significant factor in the O_3 increase associated with the cooler ERA5 temperatures. In Figure 9b this reaction

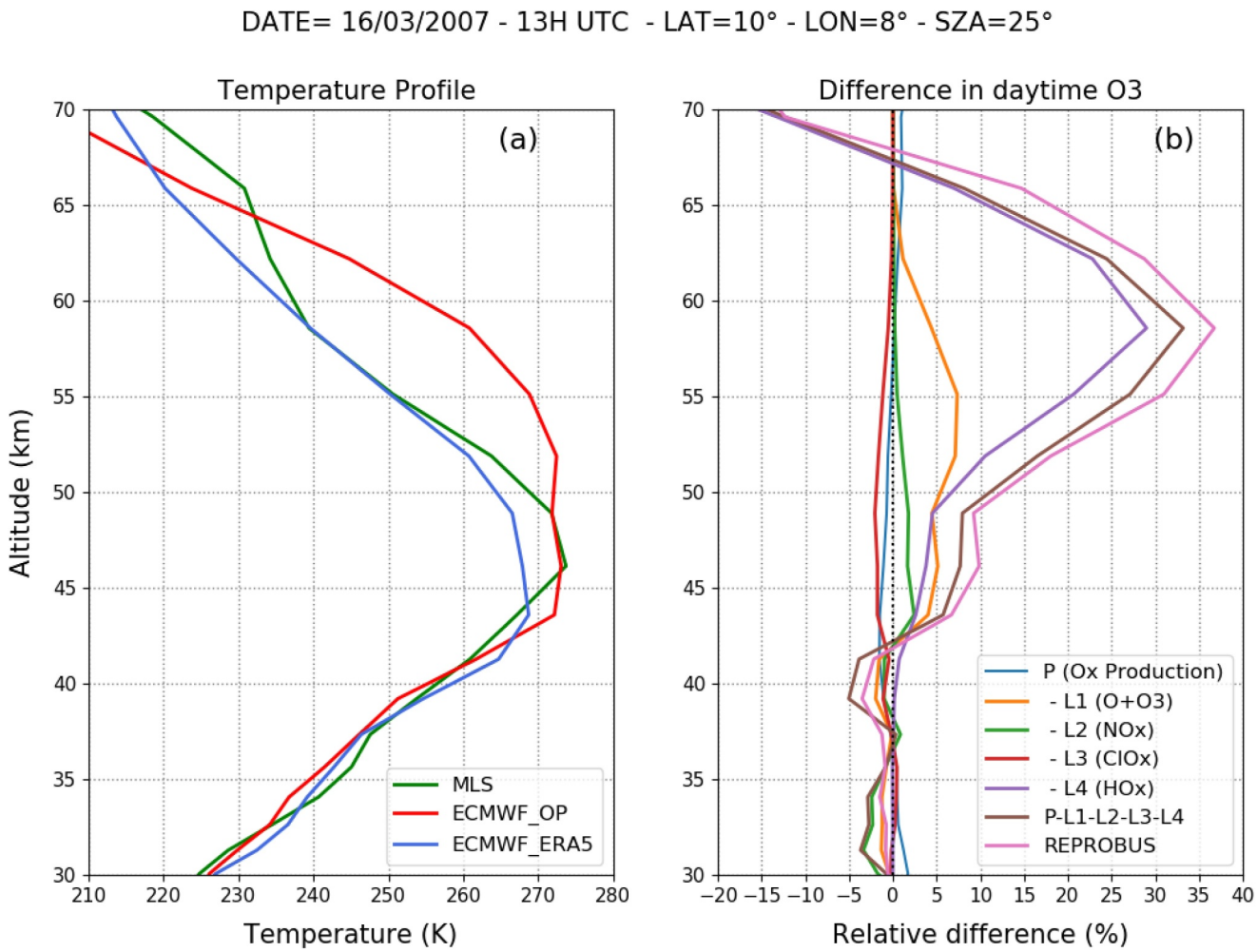

Figure 9. (a) ECMWF temperature profile (K) for 10°N 8°E on 16 March 2007 at 13UT. Red and blue curves represent operational analysis (ECMWF_OP) and ERA5 reanalysis, respectively. The nearest MLS temperature profile is also indicated in green. (b) The difference in daytime O_3 (%, pink) between the REPROBUS simulations driven by ECMWF operational analysis and ERA5 reanalysis is compared to the relative change predicted by a linearized expression of the O_x equilibrium (brown). P represents the contribution from the O_x production, whereas the L terms show the contribution from each O_x loss process (note the negative sign).

explains about half of the O_3 increase at 48 km and becomes the main contributor near the stratopause and below. However, in this altitude range the temperature effect is not sufficient to completely eliminate the O_3 deficit in the model, which remains visible in Figure 8a.

4.4. On the Remaining O_3 Deficit at 35–45 km

While the ozone deficit may be almost completely eliminated in the mesosphere by the use of appropriate temperatures, in our model there remains a deficit of 10%–15% in the stratosphere around 35–45 km. Our work thus joins the numerous studies that have documented the historical problem of model-calculated ozone deficit in the upper stratosphere (e.g., Grooß et al., 1999; Khosravi et al., 1998; Remsberg et al., 2007; Siskind et al., 1995). In our model, the deficit resists the use of the latest kinetic data, including the important channel of the ClO + OH → HCl + O_2 reaction, identified by Khosravi et al. (1998). To make progress on this issue, we have revisited, for the first time with a three-dimensional model, the possibility of an extra source of ozone produced by highly vibrationally excited oxygen, as theorized by Price et al. (1993) and Miller et al. (1994). The proposed additional ozone production mechanism is given by the following scheme, where $O_2(^3\Sigma_g^-, v \geq 26)$ is molecular oxygen in vibrationally excited state $v \geq 26$:

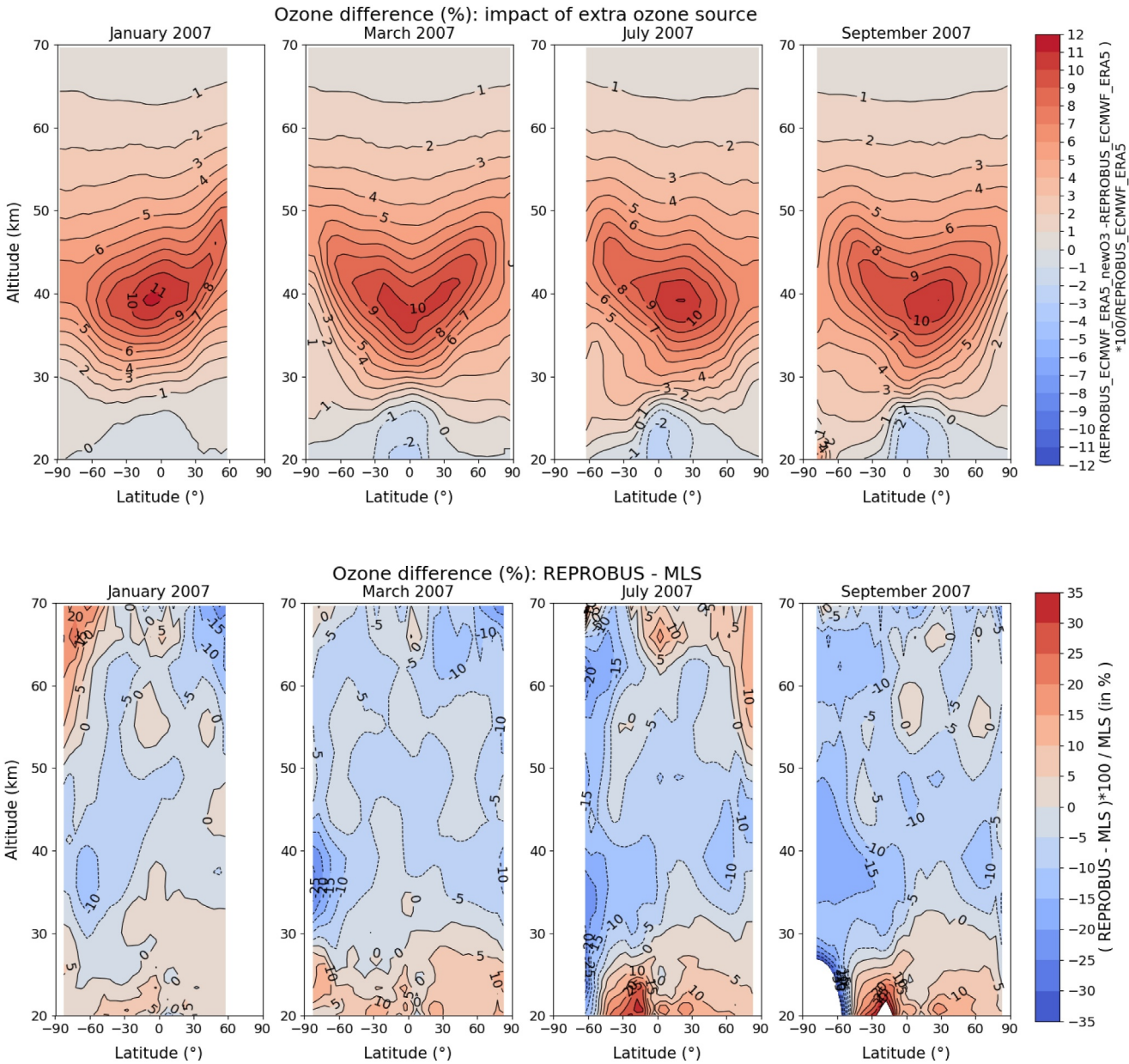

Figure 10. Top: Increase in O_3 (%) in REPROBUS when including the extra production of O_3 from vibrationally excited oxygen $O_2(^3\Sigma_g^-, v \geq 26)$. Bottom: difference (%) between REPROBUS including this extra production of O_3 and MLS. Winds are temperatures are driven by ECMWF ERA5 reanalysis. The difference is calculated as (REPROBUS-MLS)/MLS × 100. From left to right: January, March, July and September 2007 during daytime (SZA < 85°).

$$O_3 + h\nu\ (\lambda < 243\ \text{nm}) \rightarrow O_2\left(^3\Sigma_g^-, v \geq 26\right) + O\left(^3P\right) \quad (3)$$

$$O_2\left(^3\Sigma_g^-, v \geq 26\right) + O_2\left(^3\Sigma_g^-, v = 0\right) \rightarrow O_3 + O\left(^3P\right) \quad (4)$$

The quantum yield for $O_2(^3\Sigma_g^-, v \geq 26)$ production from O_3 photolysis consistently decreases with wavelength from about 7.3% at 193 nm (Stranges et al., 1995) to 0.06% at 240 nm (Geiser et al., 2000). We used these laboratory measurements and a third order polynomial fit to define in REPROBUS a wavelength-dependent function of the quantum for $O_2(^3\Sigma_g^-, v \geq 26)$ production.

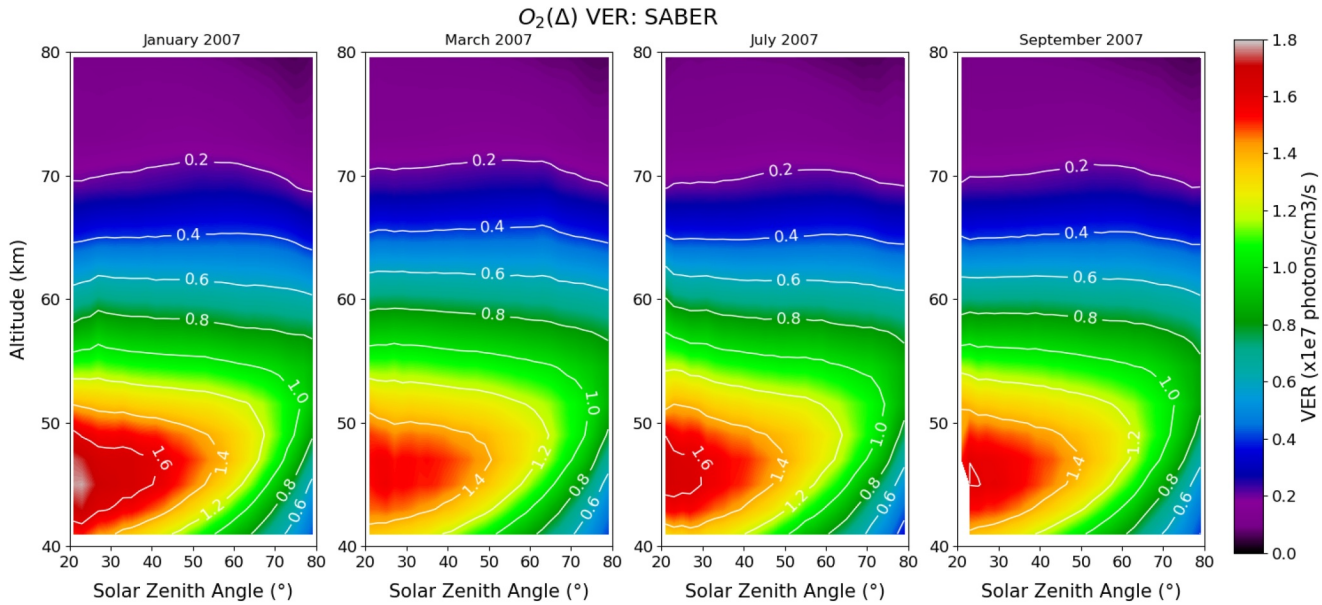

Figure 11. $O_2(^1\Delta)$ volume emission rate (photons.cm^{-3}. s^{-1}) versus SZA observed by SABER. The data are averaged between 30°N and 30°S. From left to right: January, March, July and September 2007.

Regarding reaction (3), measurements performed to determine the fraction of $O_2(^3\Sigma_g^-, v \geq 26)$ molecules that undergo vibrational relaxation to state $v-1$ clearly indicate the presence of a "dark" channel, consistent with a chemical reaction forming O_3 (Rogaski et al., 1995; Toumi et al., 1996). Unexpected O and O_3 production was also observed in the effluent of He/O_2 microplasma jet emanating into ambient air, which could be explained by reaction (4) (Ellerweg et al., 2012). In our model experiment, we considered that all $O_2(^3\Sigma_g^-, v \geq 26)$ formed by O_3 photolysis lead ultimately to the formation of O and O_3.

Figure 10 (top) shows the increase in O_3 when reactions (3) and (4) are implemented in the model. The change relative to the simulation with standard chemistry is essentially located between 35 and 45 km with a maximum of about +10% at 40 km in the tropics. This result is in good agreement with those of Miller et al. (1994) and Toumi et al. (1996) who first modeled the potential impact of vibrationally excited oxygen on stratospheric ozone. In REPROBUS, this process allows to reduce the O_3 deficit in the desired altitude range. The agreement with MLS observations is notably improved at low latitudes, where the remaining deficit is now of the order of 5%–10% between 40 and 45 km (Figure 10, bottom). The production of O_3 by vibrationally excited oxygen therefore remains a possible explanation to reduce the historical ozone deficit noted in the models. However, as this process has not been fully demonstrated experimentally, the results obtained here should still be treated with caution.

4.5. O_2 ($^1\Delta$) Dayglow

In the light of the results obtained above, we finally compare the $O_2(^1\Delta)$ dayglow modeled by REPROBUS to SABER observations. We first consider the vertical distribution of the $O_2(^1\Delta)$ volume emission rate (VER, in photons. cm^{-3}. s^{-1}), then the vertically integrated $O_2(^1\Delta)$ dayglow (in photons. cm^{-2}. s^{-1}. sr^{-1}) that will be main retrieved quantity in the 1.27 μm channel of Microcarb.

4.5.1. O_2 ($^1\Delta$) Volume Emission Rate

Figures 11 and 12 show respectively the $O_2(^1\Delta)$ volume emission rate measured by SABER between 40 and 80 km and calculated by REPROBUS in its configuration forced by the ECMWF operational analysis. The VER is averaged in the 30°N–30°S latitude band and is represented according to altitude and SZA. At first order, the model correctly reproduces the airglow maximum around 45 km, whose intensity decreases and altitude increases with the SZA. The relative difference between SABER and REPROBUS (Figure 12, bottom) shows that the model tends to overestimate the $O_2(^1\Delta)$ dayglow below the emission peak between 40 and 45 km. Above the peak, the model underestimates the $O_2(^1\Delta)$ dayglow, with a maximum difference of −25% to −30% around

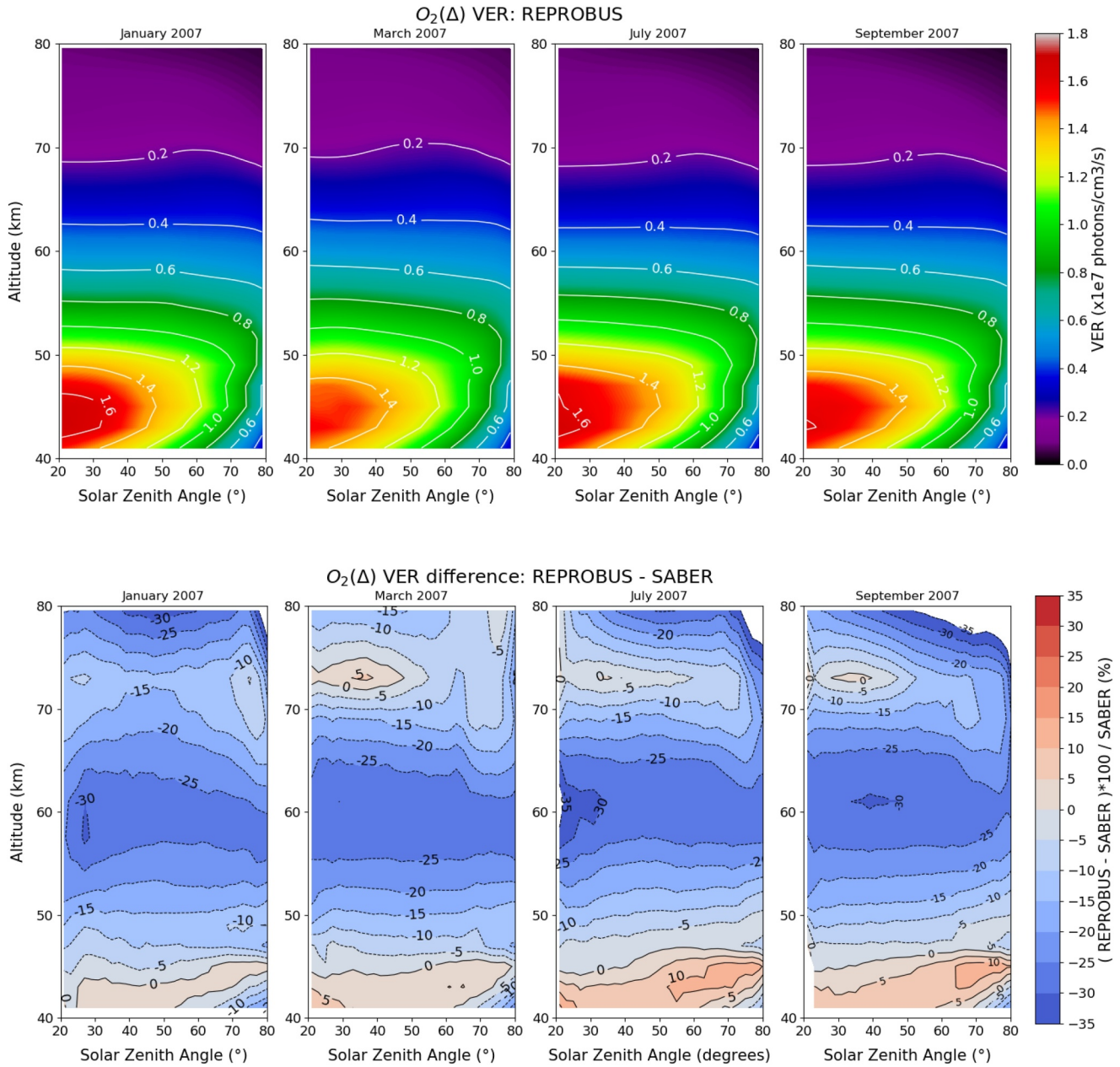

Figure 12. Top: $O_2(^1\Delta)$ volume emission rate (photons.cm^{-3}. s^{-1}) versus SZA calculated by REPROBUS with the ECMWF operational analysis. Bottom: difference (%) with SABER. The data are averaged between 30°N and 30°S. The difference is calculated as (REPROBUS - SABER)/SABER x100. From left to right: January, March, July and September 2007.

60 km. This bias, which confirms the results of Bertaux et al. (2020), is consistent with the lack of ozone of the same amplitude identified in the model in Figure 3.

When it is forced by the ERA5 reanalysis, REPROBUS calculates a more intense $O_2(^1\Delta)$ dayglow at all levels between 45 and 55 km (Figure 13). Logically, the changes in the VER compared with that obtained with the operational analyses reflect those already noted for ozone. The increase in VER is directly linked to the increase in modeled ozone, which in turn results from the lower temperatures of ERA5. As a result, the agreement with SABER is much improved, with a difference generally between +5% and −5% in the altitude range where the VER is most intense, between 40 and 60 km (Figure 13). In particular, the significant underestimation of the VER (−30%) obtained with the operational analyses around 60 km is almost completely eliminated with ERA5.

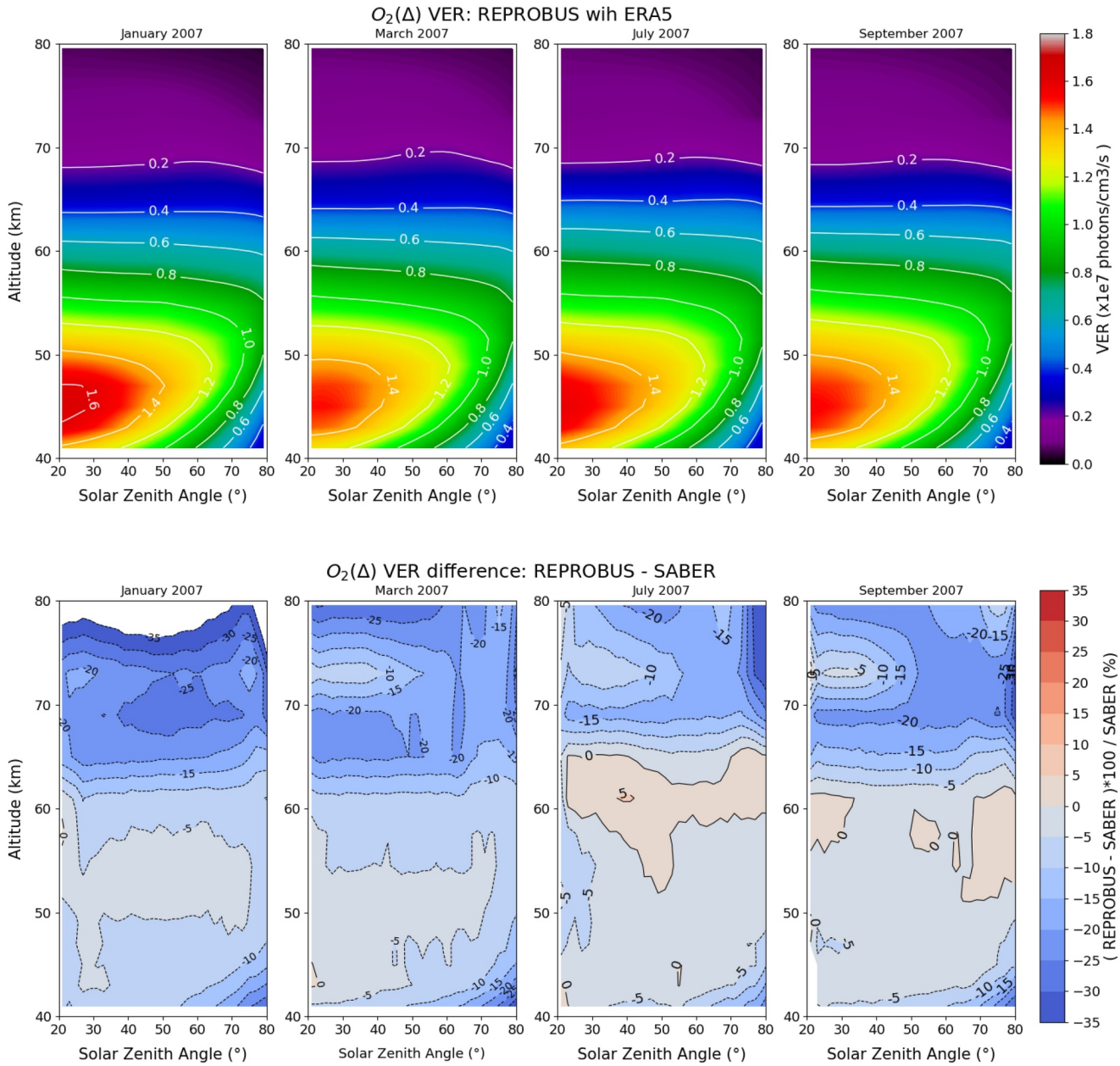

Figure 13. Top: $O_2(^1\Delta)$ volume emission rate (photons.cm^{-3}. s^{-1}) versus SZA calculated by REPROBUS with the ECMWF ERA5 reanalysis. Bottom: difference (%) with SABER. The data are averaged between 30°N and 30°S. The difference is calculated as (REPROBUS - SABER)/SABER × 100. From left to right: January, March, July and September 2007.

The only altitudes where ERA5 shows no significant improvement over operational analyses are above 65 km in January and March (70 km in July and September), where the VER is underestimated by the model by around −10% to −20%. This bias is difficult to address because of the proximity of the top of the IFS model and the absence of temperature data to assimilate. Nevertheless, the $O_2(^1\Delta)$ dayglow is small above 70 km and represents only around ∼3% of the vertically integrated dayglow measured in nadir geometry.

4.5.2. Vertically Integrated $O_2(^1\Delta)$ Dayglow

To simulate the $O_2(^1\Delta)$ dayglow as viewed by a satellite from nadir, we have integrated vertically the VER measured by SABER and calculated by REPROBUS. In both cases the integration is performed from 40 km, the lowest altitude where the VER is retrieved by SABER, up to 80 km corresponding to the uppermost level of

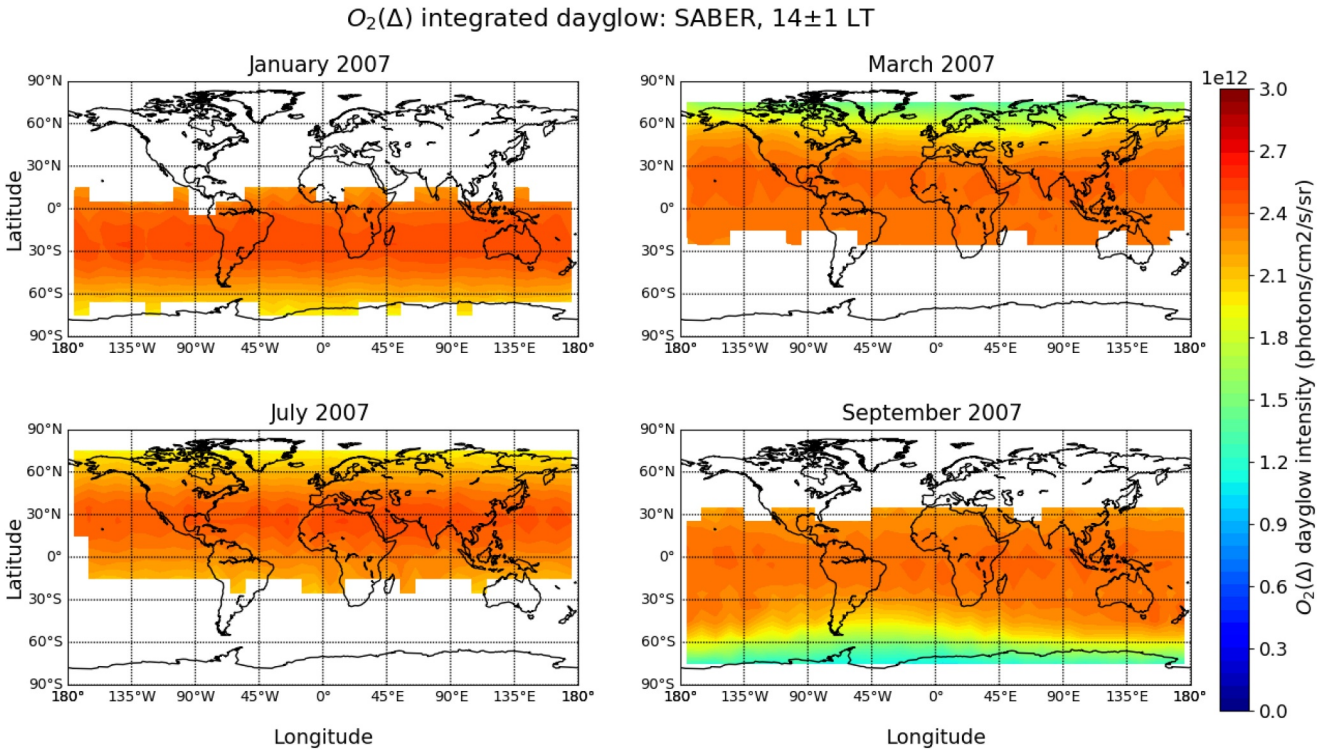

Figure 14. $O_2(^1\Delta)$ dayglow integrated between 40 and 80 km (photons.cm^{-2}. s^{-1}. sr^{-1}) measured at 14 ± 1 LT by SABER. Left to right and top to bottom: January, March, July, and September 2007.

REPROBUS. Figure 14 presents maps of the vertically integrated $O_2(^1\Delta)$ dayglow obtained from SABER. The data are monthly averaged and are restricted to the 14 ± 1 LT window in order to filter out the variations with local time. This condition on local time, together with SABER observing geometry and the yaw maneuver performed by TIMED every 60 days, limits the latitudinal coverage of the data for a given month. As already shown by Bertaux et al. (2020) from the SCIAMACHY data, the dayglow maps in Figure 14 are almost independent of longitude. At a given local time, the $O_2(^1\Delta)$ brightness is lower at high latitudes due to the larger SZA. The region of maximum brightness moves with the season and follows the latitude of the sub-solar point. This illustrates again the importance of the SZA as the main driver of the vertically integrated $O_2(^1\Delta)$ airglow intensity. The only exception to this rule can be seen in September 2007 near 60°S, when the displacement off the pole of the ozone-poor polar vortex caused a local reduction in the $O_2(^1\Delta)$ airglow over the 45°W sector.

Figure 15 maps the $O_2(^1\Delta)$ brightness calculated by REPROBUS when forced by the ECMWF operational analysis and the ERA5 reanalysis, respectively. As expected, the high latitudes in winter, not sampled by SABER, show a sharp reduction in the $O_2(^1\Delta)$ brightness calculated by the model, dropping to zero in the polar night regions. At low and mid-latitudes, REPROBUS shows a pattern identical to that of SABER, with the quasi-absence of longitudinal variations and the seasonal displacement of the $O_2(^1\Delta)$ emission maximum along the sub-solar point. In September 2007 near 60°S, the local reduction in the $O_2(^1\Delta)$ emission associated with the displacement of the polar vortex is also reproduced by REPROBUS.

The relative difference between SABER and REPROBUS forced by the ECMWF operational analysis is shown in Figure 16 (left). It can be seen that the model underpredicts the $O_2(^1\Delta)$ brightness at all latitudes and seasons. On an annual average, the brightness deficit in REPROBUS compared with SABER is −11.0 ± 2.7%. This result is consistent with the −13% deficit found by Bertaux et al. (2020) who used a limited set (April 2007) of SCIAMACHY nadir-viewing observations as reference. In Figure 16 (right), the use of ERA5 reanalysis to drive REPROBUS leads to a systematic increase in the $O_2(^1\Delta)$ brightness. This result is expected because of the strong increase in VER previously seen in the 50–70 km layer. As a result, although still slightly underestimated, the integrated $O_2(^1\Delta)$ airglow calculated with the ERA5 reanalysis is significantly closer to SABER than that calculated with the operational analysis. On a global and annual average, the difference between REPROBUS and

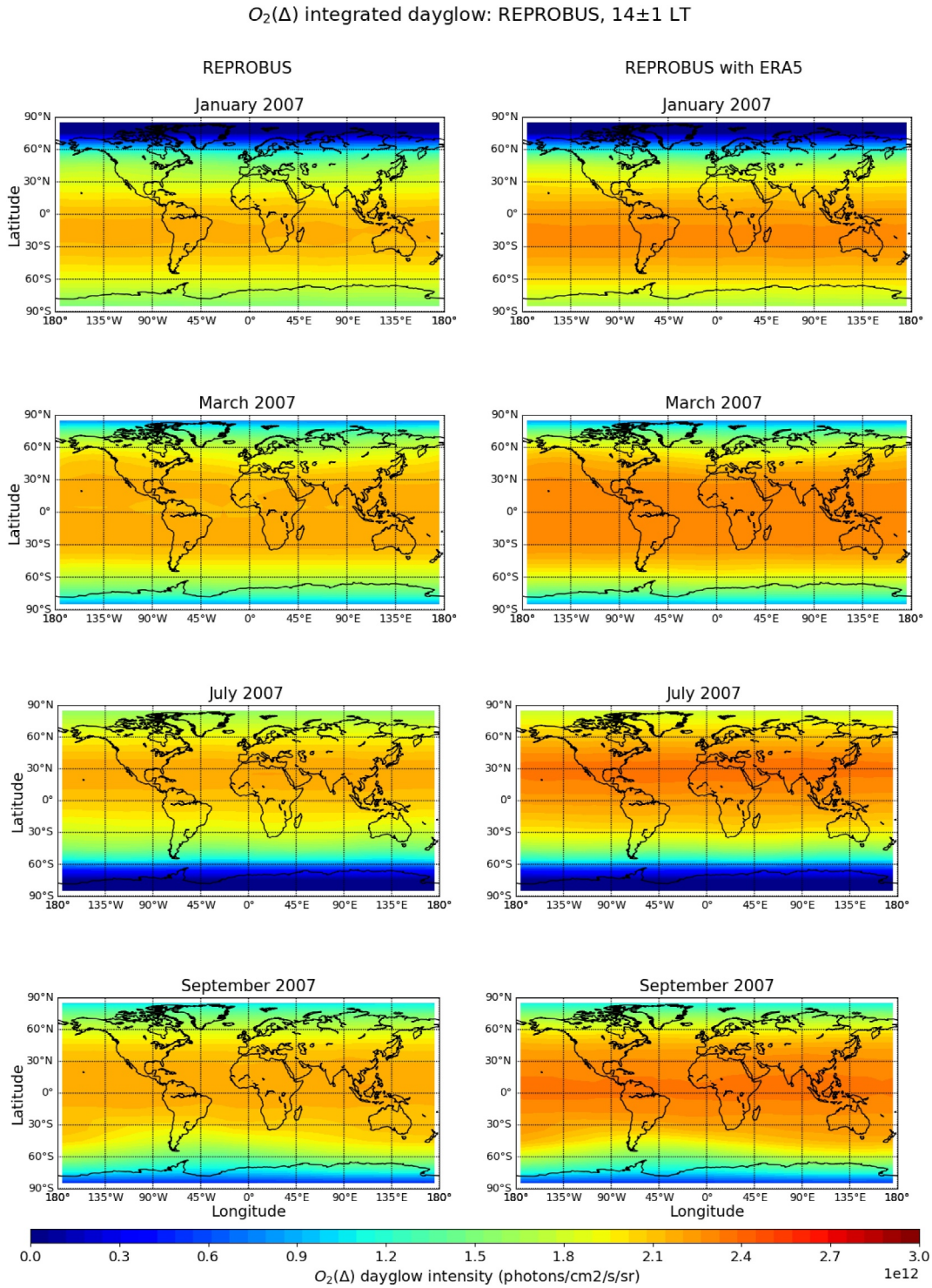

Figure 15. $O_2(^1\Delta)$ dayglow integrated between 40 and 80 km (photons.cm^{-2}. s^{-1}. sr^{-1}) calculated at 14 ± 1 LT by REPROBUS with the ECMWF operational analysis (left) and REPROBUS with the ERA5 reanalysis (right). Top to bottom: January, March, July, and September 2007.

SABER drops to −4.2 ± 2.8%. The fact that this difference remains negative can be attributed to the lack of ozone and $O_2(^1\Delta)$ VER that persists between 35 and 45 km. Nevertheless, a major part of the initial bias in Figure 16 (left) has been eliminated by using the colder ERA5 temperatures in the mesosphere. Even when integrated

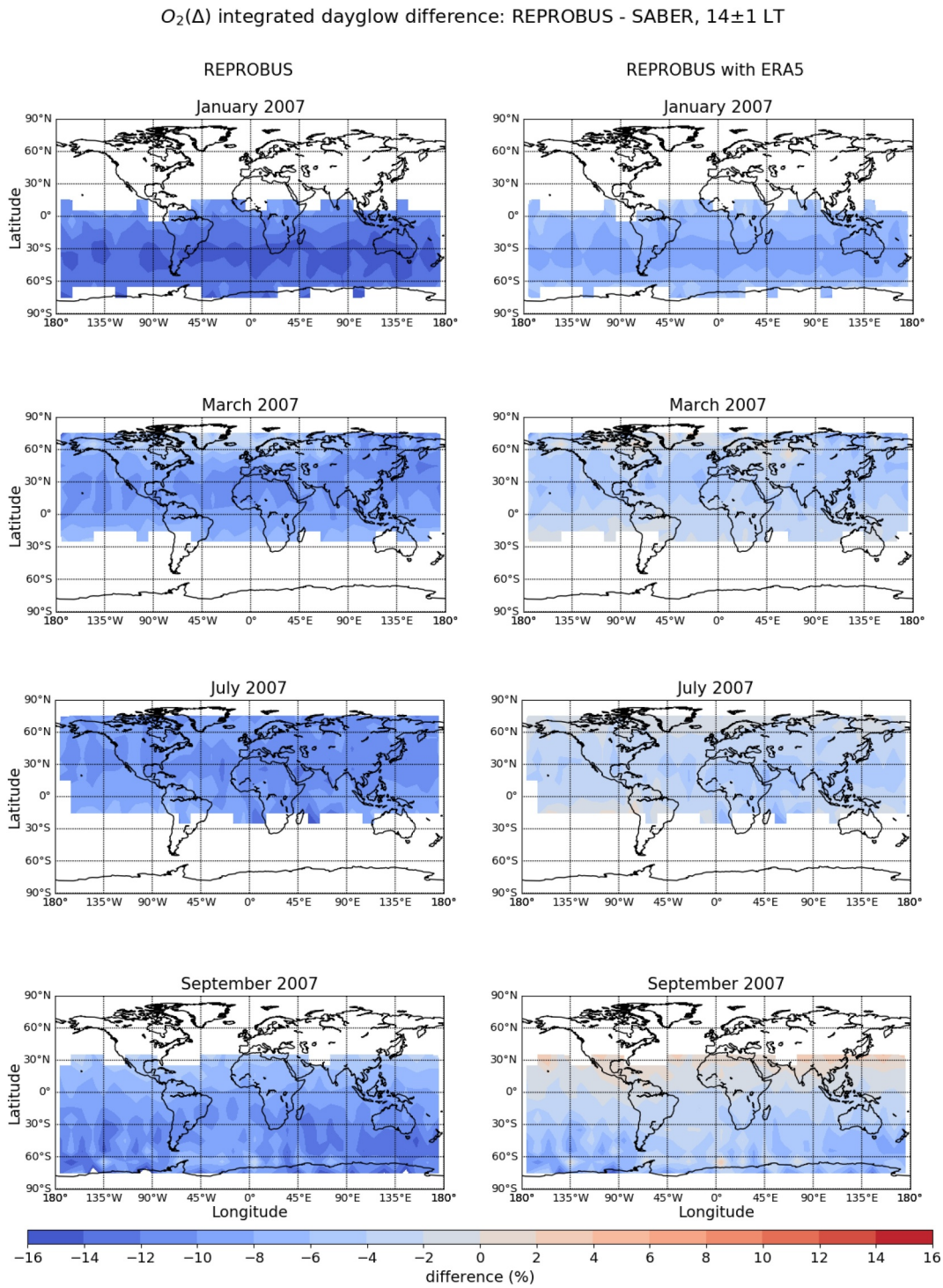

Figure 16. Difference (%) between the $O_2(^1\Delta)$ dayglow calculated by REPROBUS with the ECMWF operational analysis and measured by SABER (left) and calculated by REPROBUS with the ECMWF ERA5 reanalysis and measured by SABER (right). Data are integrated between 40 and 80 km at 14 ± 1 LT. The difference is calculated as (REPROBUS-SABER)/SABER × 100. Top to bottom: January, March, July, and September 2007.

vertically, in order to simulate a measurement in nadir geometry, the use of accurate temperatures in the mesosphere is therefore a key factor for an accurate estimate of the $O_2(^1\Delta)$ brightness with a chemical model. In addition to the ERA5 temperatures, the inclusion of the effect of vibrationally excited oxygen as envisaged in Section 4.4 reduces the difference between the model and SABER to $-1.6 \pm 2.9\%$.

5. Conclusions

In this work, we investigated the three-dimensional climatology of the $O_2(^1\Delta)$ dayglow as calculated by a state-of-the-art chemistry-transport model. On the basis of the MLS data, we have established the causes of the $O_2(^1\Delta)$ dayglow deficit in the simulations carried out with the same model by Bertaux et al. (2020). This lack of dayglow is clearly associated with a significant ozone deficit in the model, particularly marked (-20% to -30%) near the stratopause and in the lower mesosphere (45–60 km).

We find that the ozone deficit is due to excessively high temperatures (+15K) of the nominal meteorological analyses used to drive the model in the mesosphere. The use of lower analyzed temperatures (ERA5), in better agreement with the observations, slows down both the HO_x catalytic cycles (by shifting the equilibrium between O and O_3) and the Chapman O_x loss reaction. These two factors combined lead to an almost total elimination of the O_3 and $O_2(^1\Delta)$ deficits in the lower mesosphere.

Around 35–45 km, however, the model still has a negative ozone bias of around -10% to -15% compared with observations. This problem is a continuation of the "historical" ozone deficit noted in the middle stratosphere by numerous past studies, and does not seem to be resolved by the use of the most recent kinetic data. We have tested the additional production of ozone by vibrationally excited oxygen, as theorized by Price et al. (1993). By increasing ozone by nearly 10% in the desired altitude range, this process remains an attractive solution to the modeled ozone deficit in the stratosphere. However, its existence remains somewhat speculative in the absence of full experimental demonstration.

We simulated the vertically integrated $O_2(^1\Delta)$ dayglow to reproduce the observing conditions of Microcarb or any other instrument covering the 1.27 μm band in nadir geometry. When our three-dimensional model is forced by the ECMWF operational analysis of 2007, the calculated $O_2(^1\Delta)$ dayglow is biased low with a mean difference of $-11.0 \pm 2.7\%$ relative to the SABER measurements. However, as with ozone, we find that this result is very sensitive to mesospheric temperatures: the use of the cooler ERA5 reanalysis to drive the model reduces the bias by a factor of nearly 3, for an average result of $-4.2 \pm 2.8\%$. The slight underestimation that persists with ERA5 is mostly attributable to the uncorrected negative bias of ozone between 35 and 45 km.

Future space missions using the 1.27 μm band to measure the air column and ultimately CO_2 may not have the spectral resolution required to disentangle the $O_2(^1\Delta)$ emission from the $O_2(^1\Delta)$ absorption (Bertaux et al., 2020). In this case, a chemistry-transport model similar to that used here will be required to calculate the $O_2(^1\Delta)$ theoretical emission, and remove it from the observed spectra. Our work shows that particular attention needs to be paid to the accuracy of the mesospheric temperatures used for this calculation. As meteorological analyses suffer cruelly from a lack of data assimilated in the mesosphere, the quality of the underlying weather prediction model (IFS in the case of ECMWF) in that region plays a decisive role in the quality of the representation of the $O_2(^1\Delta)$ dayglow.

Data Availability Statement

The MLS, SABER and Model data presented in this study are available in this in-text data citation reference: Diouf (2023). Global SABER data are available on the dedicated SABER website: https://saber.gats-inc.com/. The MLS data products are available on https://search.earthdata.nasa.gov/search?fi=MLS.

References

Acknowledgments
M. M. N. D. gratefully acknowledges support from the Centre National d'Etudes Spatiales (CNES) and ACRI-St. The authors also thank the Jet Propulsion Lab (JPL) for access to the Aura MLS data and the SABER (ftp://saber.gats-inc.com/) data processing and science teams.

Atkinson, R., Baulch, D. L., Cox, R. A., Crowley, J. N., Hampson Jr., R. F., Kerr, J. A., & Troe, J. (2005). Summary of evaluated kinetic and photochemical data for atmospheric chemistry. *IUPAC Subcommittee on gas kinetic data evaluation for atmospheric chemistry*, *20*. http://rpw.chem.ox.ac.uk/IUPACsumm_web_latest.pdf

Baluja, K. L., & Zeippen, C. J. (1988). Excitation energies and oscillator strengths for the allowed transitions 2p4 3P to 2s2p5 3P0 and 2p4 1D, 1S to 2s2p5 1P0 in the OI isoelectronic sequence. *Journal of Physics B: Atomic, Molecular and Optical Physics*, *21*(1), 15–24. https://doi.org/10.1088/0953-4075/21/1/002

Bechtold, P., Orr, A., Morcrette, J.-J., Engelen, R., Flemming, J., & Janiskova, M. (2009). Improvements in the stratosphere and mesosphere of the IFS. *ECMWF newsletter*, *120*, 22–31.

Bertaux, J. L., Hauchecorne, A., Lefèvre, F., Bréon, F. M., Blanot, L., Jouglet, D., et al. (2020). The use of the 1.27 μm O_2 absorption band for greenhouse gas monitoring from space and application to MicroCarb. *Atmospheric Measurement Techniques*, *13*(6), 3329–3374. https://doi.org/10.5194/amt-13-3329-2020

Bovensmann, H., Burrows, J. P., Buchwitz, M., Frerick, J., Noel, S., Rozanov, V. V., et al. (1999). SCIAMACHY: Mission objectives and measurement modes. *Journal of the Atmospheric Sciences*, *56*(2), 127–150. https://doi.org/10.1175/1520-0469(1999)056<0127:smoamm>2.0.co;2

Burkholder, J. A., Sander, S. P., Abbatt, J. P. D., Barker, J. R., Cappa, C., Crounse, J. D., & Wine, P. H. (2019). *Chemical Kinetics and photochemical data for use in atmospheric studies evaluation No. 19, JPL publication 19-5, NASA panel for data evaluation. National aeronautics and space administration, jet propulsion laboratory*. California Institute of Technology. Retrieved from https://jpldataeval.jpl.nasa.gov/pdf/NASA-JPL%20Evaluation%2019-5.pdf

Burrows, J. P., Hölzle, E., Goede, A. P. H., Visser, H., & Fricke, W. (1995). SCIAMACHY—Scanning imaging absorption spectrometer for atmospheric chartography. *Acta Astronautica*, *35*(7), 445–451. https://doi.org/10.1016/0094-5765(94)00278-T

Butler, D. M. (1978). The uncertainty in ozone calculations by a stratospheric photochemistry model. *Geophysical Research Letters*, *5*(9), 769–772. https://doi.org/10.1029/GL005i009p00769

Canty, T., Pickett, H. M., Salawitch, R. J., Jucks, K. W., Traub, W. A., & Waters, J. W. (2006). Stratospheric and mesospheric HOx: Results from Aura MLS and FIRS-2. *Geophysical Research Letters*, *33*(12). https://doi.org/10.1029/2006GL025964

Cariolle, D., Moinat, P., Teyssèdre, H., Giraud, L., Josse, B., & Lefèvre, F. (2017). ASIS v1. 0: An adaptive solver for the simulation of atmospheric chemistry. *Geoscientific Model Development*, *10*(4), 1467–1485. https://doi.org/10.5194/gmd-10-1467-2017

Clancy, R. T., Sandor, B. J., Rusch, D. W., & Muhleman, D. O. (1994). Microwave observations and modeling of O_3, H_2O, and HO_2 in the mesosphere. *Journal of Geophysical Research*, *99*(D3), 5465–5473. https://doi.org/10.1029/93JD03471

Conway, R. R., Stevens, M. H., Cardon, J. G., Zasadil, S. E., Brown, C. M., Morrill, J. S., & Mount, G. H. (1996). Satellite measurements of hydroxyl in the mesosphere. *Geophysical Research Letters*, *23*(16), 2093–2096. https://doi.org/10.1029/96GL01401

Conway, R. R., Summers, M. E., Stevens, M. H., Cardon, J. G., Preusse, P., & Offermann, D. (2000). Satellite observations of upper stratospheric and mesospheric OH: The HOx dilemma. *Geophysical Research Letters*, *27*(17), 2613–2616. https://doi.org/10.1029/2000GL011698

Dakermanji, G., Butler, M., Carlsson, P. U., & Temkin, D. (1997). The thermosphere, ionosphere, mesosphere energetics and dynamics (TIMED) spacecraft power system. In *IECEC-97 proceedings of the thirty-second intersociety energy conversion engineering conference (cat. No. 97CH6203)* (Vol. 1, pp. 544–549). IEEE. Retrieved from https://ieeexplore.ieee.org/document/659248

Diouf, M. (2023). Data of the article: Three-dimensional modeling of the O_2 (1Δ) dayglow and implications for ozone in the middle atmosphere [Dataset]. *Mendeley Data*. https://doi.org/10.17632/25FDMBCGGP.1

Drouin, B. J., Benner, D. C., Brown, L. R., Cich, M. J., Crawford, T. J., Devi, V. M., et al. (2017). Multispectrum analysis of the oxygen A-band. *Journal of Quantitative Spectroscopy and Radiative Transfer*, *186*, 118–138. https://doi.org/10.1016/j.jqsrt.2016.03.037

Ehard, B., Malardel, S., Dörnbrack, A., Kaifler, B., Kaifler, N., & Wedi, N. (2017). Comparing ECMWF high-resolution analyses with lidar temperature measurements in the middle atmosphere. *Quarterly Journal of the Royal Meteorological Society*, *144*(712), 633–640. https://doi.org/10.1002/qj.3206

Ellerweg, D., Von Keudell, A., & Benedikt, J. (2012). Unexpected O and O_3 production in the effluent of He/O_2 microplasma jets emanating into ambient air. *Plasma Sources Science and Technology*, *21*(3), 034019. https://doi.org/10.1088/0963-0252/21/3/034019

Eluszkiewicz, J., & Allen, M. (1993). A global analysis of the ozone deficit in the upper stratosphere and lower mesosphere. *Journal of Geophysical Research*, *98*(D1), 1069–1082. https://doi.org/10.1029/92JD01912

Englert, C. R., Stevens, M. H., Siskind, D. E., Harlander, J. M., & Roesler, F. L. (2010). Spatial heterodyne imager for mesospheric radicals on STPSat-1. *Journal of Geophysical Research*, *115*(D20). https://doi.org/10.1029/2010JD014398

Englert, C. R., Stevens, M. H., Siskind, D. E., Harlander, J. M., Roesler, F. L., Pickett, H. M., et al. (2008). First results from the spatial heterodyne imager for mesospheric radicals (SHIMMER): Diurnal variation of mesospheric hydroxyl. *Geophysical Research Letters*, *35*(19). https://doi.org/10.1029/2008GL035420

Evans, W. F. J., Hunten, D. M., Llewellyn, E. J., & Jones, A. V. (1968). Altitude profile of the infrared atmospheric system of oxygen in the dayglow. *Journal of Geophysical Research*, *73*(9), 2885–2896. https://doi.org/10.1029/JA073i009p02885

Frankenberg, C., Pollock, R., Lee, R. A. M., Rosenberg, R., Blavier, J. F., Crisp, D., et al. (2015). The orbiting carbon observatory (OCO-2): Spectrometer performance evaluation using pre-launch direct sun measurements. *Atmospheric Measurement Techniques*, *8*(1), 301–313. https://doi.org/10.5194/amt-8-301-2015

Frederick, J. E., Guenther, B. W., Hays, P. B., & Heath, D. F. (1978). Ozone profiles and chemical loss rates in the tropical stratosphere deduced from backscatter ultraviolet measurements. *Journal of Geophysical Research*, *83*(C2), 953–958. https://doi.org/10.1029/JC083iC02p00953

Froidevaux, L., Allen, M., & Yung, Y. L. (1985). A critical analysis of ClO and O_3 in the mid-latitude stratosphere. *Journal of Geophysical Research*, *90*(D7), 12999–13029. https://doi.org/10.1029/JD090iD07p12999

Froidevaux, L., Jiang, Y. B., Lambert, A., Livesey, N. J., Read, W. G., Waters, J. W., et al. (2008). Validation of Aura microwave limb sounder stratospheric ozone measurements. *Journal of Geophysical Research*, *113*(D15), D15S20. https://doi.org/10.1029/2007JD008771

Geiser, J. D., Dylewski, S. M., Mueller, J. A., Wilson, R. J., Toumi, R., & Houston, P. L. (2000). The vibrational distribution of O_2 ($X^3\Sigma_g^-$) produced in the photodissociation of ozone between 226 and 240 and at 266 nm. *The Journal of Chemical Physics*, *112*(3), 1279–1286. https://doi.org/10.1063/1.480679

Gibson, S. T., Gies, H. P. F., Blake, A. J., McCoy, D. G., & Rogers, P. J. (1983). Temperature dependence in the Schumann-Runge photoabsorption continuum of oxygen. *Journal of Quantitative Spectroscopy and Radiative Transfer*, *30*(5), 385–393. https://doi.org/10.1016/0022-4073(83)90101-2

Grooß, J. U., Müller, R., Becker, G., McKenna, D. S., & Crutzen, P. J. (1999). The upper stratospheric ozone budget: An update of calculations based on HALOE data. *Journal of Atmospheric Chemistry*, *34*(2), 171–183. https://doi.org/10.1023/a:1006290927549

Hersbach, H., Bell, B., Berrisford, P., Hirahara, S., Horányi, A., Muñoz-Sabater, J., et al. (2020). The ERA5 global reanalysis. *Quarterly Journal of the Royal Meteorological Society*, *146*(730), 1999–2049. https://doi.org/10.1002/qj.3803

Jiang, Y. B., Froidevaux, L., Lambert, A., Livesey, N. J., Read, W. G., Waters, J. W., et al. (2007). Validation of Aura microwave limb sounder ozone by ozonesonde and lidar measurements. *Journal of Geophysical Research*, *112*(D24). https://doi.org/10.1029/2007JD008776

Jones, W. H., & Welker, J. (1970). Mid-latitude rocket observations of the altitude profile of the O2/a/1 Delta g//-/X/3 Sigma g plus//transition. (No. NASA-TM-X-65606).

Jonsson, A. I., De Grandpre, J., Fomichev, V. I., McConnell, J. C., & Beagley, S. R. (2004). Doubled CO2-induced cooling in the middle atmosphere: Photochemical analysis of the ozone radiative feedback. *Journal of Geophysical Research*, *109*(D24). https://doi.org/10.1029/2004jd005093

Jucks, K. W., Johnson, D. G., Chance, K. V., Traub, W. A., Margitan, J. J., Osterman, G. B., et al. (1998). Observations of OH, HO_2, H_2O, and O_3 in the upper stratosphere: Implications for HOx photochemistry. *Geophysical Research Letters*, *25*(21), 3935–3938. https://doi.org/10.1029/1998GL900009

Khosravi, R., Brasseur, G. P., Smith, A. K., Rusch, D. W., Waters, J. W., & Russell III, J. M. (1998). Significant reduction in the stratospheric ozone deficit using a three-dimensional model constrained with UARS data. *Journal of Geophysical Research*, *103*(D13), 16203–16219. https://doi.org/10.1029/98JD01084

Kuze, A., Suto, H., Shiomi, K., Kawakami, S., Tanaka, M., Ueda, Y., et al. (2016). Update on GOSAT TANSO-FTS performance, operations, and data products after more than 6 years in space. *Atmospheric Measurement Techniques*, *9*(6), 2445–2461. https://doi.org/10.5194/amt-9-2445-2016

Lafferty, W. J., Solodov, A. M., Lugez, C. L., & Fraser, G. T. (1998). Rotational line strengths and self-pressure-broadening coefficients for the 1.27-μm, a 1 Δ g–X 3 Σ g-v= 0–0 band of O 2. *Applied Optics*, *37*(12), 2264–2270. https://doi.org/10.1364/AO.37.002264

Lefevre, F., Brasseur, G. P., Folkins, I., Smith, A. K., & Simon, P. (1994). Chemistry of the 1991–1992 stratospheric winter: Three-dimensional model simulations. *Journal of Geophysical Research*, *99*(D4), 8183–8195. https://doi.org/10.1029/93JD03476

Lefèvre, F., Figarol, F., Carslaw, K. S., & Peter, T. (1998). The 1997 Arctic ozone depletion quantified from three-dimensional model simulations. *Geophysical Research Letters*, *25*(13), 2425–2428. https://doi.org/10.1029/98GL51812

Lewis, B. R., Vardavas, I. M., & Carver, J. H. (1983). The aeronomic dissociation of water vapor by solar H Lyman α radiation. *Journal of Geophysical Research*, *88*(A6), 4935–4940. https://doi.org/10.1029/JA088iA06p04935

Livesey, N., Read, W., Wagner, P., Froidevaux, L., Santee, M., Schwartz, M., & Wu, D. L. (2020). Version 5.0 x level 2 and 3 data quality and description document.version 5.0-1.0 a. *Jet Propulsion Laboratory*. https://mls.jpl.nasa.gov/data/v5-0_data_quality_document.pdf

Livesey, N. J., Filipiak, M. J., Froidevaux, L., Read, W. G., Lambert, A., Santee, M. L., et al. (2008). Validation of Aura Microwave Limb Sounder O_3 and CO observations in the upper troposphere and lower stratosphere. *Journal of Geophysical Research*, *113*(D15). https://doi.org/10.1029/2007JD008805

Llewellyn, E. J., Lloyd, N. D., Degenstein, D. A., Gattinger, R. L., Petelina, S. V., Bourassa, A. E., & Nordh, L. (2004). The OSIRIS instrument on the Odin spacecraft. *Canadian Journal of Physics*, *82*(6), 411–422. https://doi.org/10.1139/p04-00

Madronich, S., & Flocke, S. (1998). *The role of solar radiation in atmospheric chemistry* (pp. 1–26). Springer-Verlag.

Marlton, G., Charlton-Perez, A., Harrison, G., Polichtchouk, I., Hauchecorne, A., Keckhut, P., et al. (2021). Using a network of temperature lidars to identify temperature biases in the upper stratosphere in ECMWF reanalyses. *Atmospheric Chemistry and Physics*, *21*(8), 6079–6092. https://doi.org/10.5194/acp-21-6079-2021

McElroy, M. B., & Salawitch, R. J. (1989). Changing composition of the global stratosphere. *Science*, *243*(4892), 763–770. https://doi.org/10.1126/science.243.4892.763

Miller, R. L., Suits, A. G., Houston, P. L., Toumi, R., Mack, J. A., & Wodtke, A. M. (1994). The" ozone deficit" problem: O_2 (X, v≥ 26)+ O (3 P) from 226-nm ozone photodissociation. *Science*, *265*(5180), 1831–1838. https://doi.org/10.1126/science.265.5180.1831

Mlynczak, M. G. (1997). Energetics of the mesosphere and lower thermosphere and the SABER experiment. *Advances in Space Research*, *20*(6), 1177–1183. https://doi.org/10.1016/S0273-1177(97)00769-2

Mlynczak, M. G., Marshall, B. T., Martin-Torres, F. J., Russell III, J. M., Thompson, R. E., Remsberg, E. E., & Gordley, L. L. (2007). Sounding of the Atmosphere using Broadband Emission Radiometry observations of daytime mesospheric O_2 (1Δ) 1.27 μm emission and derivation of ozone, atomic oxygen, and solar and chemical energy deposition rates. *Journal of Geophysical Research*, *112*(D15). https://doi.org/10.1029/2006JD008355

Mlynczak, M. G., & Russell, J. M. (1995). An overview of the SABER experiment for the TIMED mission. *Optical remote sensing of the atmosphere*, MA2. https://doi.org/10.1364/orsa.1995.ma2

Mlynczak, M. G., Solomon, S., & Zaras, D. S. (1993). An updated model for O_2 (a1Δg) concentrations in the mesosphere and lower thermosphere and implications for remote sensing of ozone at 1.27 μm. *Journal of Geophysical Research*, *98*(D10), 18639–18648. https://doi.org/10.1029/93JD01478

Natarajan, M., & Callis, L. B. (1989). Examination of stratospheric ozone photochemistry in light of recent data. *Geophysical Research Letters*, *16*(5), 473–476. https://doi.org/10.1029/GL016i005p00473

Noxon, J. F., & Jones, A. V. (1962). Observation of the (0, 0) band of the (1Δ g–3Σ g−) system of oxygen in the day and twilight airglow. *Nature*, *196*(4850), 157–158. https://doi.org/10.1038/196157a0

Ogawa, S., & Ogawa, M. (1975). Absorption cross sections of O_2 (a 1Δg) and O_2 (X 3Σg−) in the region from 1087 to 1700 Å. *Canadian Journal of Physics*, *53*(19), 1845–1852. https://doi.org/10.1139/p75-236

Pasternak, F., Bernard, P., Georges, L., & Pascal, V. (2017). (Vol. *10562*, pp. 485–497). The microcarb instrument. *International Conference on Space Optics—ICSO 2016*.

Pickett, H. M., Drouin, B. J., Canty, T., Kovalenko, L. J., Salawitch, R. J., Livesey, N. J., et al. (2006). Validation of Aura MLS HOx measurements with remote-sensing balloon instruments. *Geophysical Research Letters*, *33*(1). https://doi.org/10.1029/2005gl024048

Pickett, H. M., Drouin, B. J., Canty, T., Salawitch, R. J., Fuller, R. A., Perun, V. S., et al. (2008). Validation of Aura Microwave limb sounder OH and HO_2 measurements. *Journal of Geophysical Research*, *113*(D16). https://doi.org/10.1029/2007JD008775

Price, J. M., Mack, J. A., Rogaski, C. A., & Wodtke, A. M. (1993). Vibrational-state-specific self-relaxation rate constant. Measurements of highly vibrationally excited O_2 (ν= 19–28). *Chemical Physics*, *175*(1), 83–98. https://doi.org/10.1016/0301-0104(93)80230-7

Remsberg, E., Lingenfelser, G., Natarajan, M., Gordley, L., Marshall, B. T., & Thompson, E. (2007). On the quality of the Nimbus 7 LIMS version 6 ozone for studies of the middle atmosphere. *Journal of Quantitative Spectroscopy and Radiative Transfer*, *105*(3), 492–518. https://doi.org/10.1016/j.jqsrt.2006.12.005

Rogaski, C. A., Mack, J. A., & Wodtke, A. M. (1995). State-to-state rate constants for relaxation of highly vibrationally excited O_2 and implications for its atmospheric fate. *Faraday Discussions*, *100*, 229–251. https://doi.org/10.1039/FD9950000229

Rusch, D. W., & Eckman, R. S. (1985). Implications of the comparison of ozone abundances measured by the Solar Mesosphere Explorer to model calculations. *Journal of Geophysical Research*, *90*(D7), 12991–12998. https://doi.org/10.1029/JD090iD07p12991

Russell, J. M., Mlynczak, M. G., Gordley, L. L., Tansock Jr., J. J., & Esplin, R. W. (1999). Overview of the SABER experiment and preliminary calibration results. In *Optical spectroscopic techniques and instrumentation for atmospheric and space research III* (Vol. 3756, pp. 277–288). SPIE. Retrieved from https://digitalcommons.usu.edu/sdl_pubs/114

Sandor, B. J., & Clancy, R. T. (1998). Mesospheric HOx chemistry from diurnal microwave observations of HO2, O3, and H2O. *Journal of Geophysical Research*, *103*(D11), 13337–13351. https://doi.org/10.1029/98jd00432

Sandor, B. J., Clancy, R. T., Rusch, D. W., Randall, C. E., Eckman, R. S., Siskind, D. S., & Muhleman, D. O. (1997). Microwave observations and modeling of O_2 (1Δg) and O_3 diurnal variation in the mesosphere. *Journal of Geophysical Research*, *102*(D7), 9013–9028. https://doi.org/10.1029/96JD03585

Schwartz, M. J., Lambert, A., Manney, G. L., Read, W. G., Livesey, N. J., Froidevaux, L., et al. (2008). Validation of the Aura microwave limb sounder temperature and geopotential height measurements. *Journal of Geophysical Research*, *113*(D15). https://doi.org/10.1029/2007JD008783

Siskind, D. E., Connor, B. J., Eckman, R. S., Remsberg, E. E., Tsou, J. J., & Parrish, A. (1995). An intercomparison of model ozone deficits in the upper stratosphere and mesosphere from two data sets. *Journal of Geophysical Research*, *100*(D6), 11191–11201. https://doi.org/10.1029/95JD00366

Siskind, D. E., Froidevaux, L., Russell, J. M., & Lean, J. (1998). Implications of upper stratospheric trace constituent changes observed by HALOE for O_3 and ClO from 1992 to 1995. *Geophysical Research Letters*, *25*(18), 3513–3516. https://doi.org/10.1029/98GL02664

Siskind, D. E., Stevens, M. H., Englert, C. R., & Mlynczak, M. G. (2013). Comparison of a photochemical model with observations of mesospheric hydroxyl and ozone. *Journal of Geophysical Research: Atmospheres*, *118*(1), 195–207. https://doi.org/10.1029/2012JD017971

Solomon, S., Rusch, D. W., Thomas, R. J., & Eckman, R. S. (1983). Comparison of mesospheric ozone abundances measured by the Solar Mesosphere Explorer and model calculations. *Geophysical Research Letters*, *10*(4), 249–252. https://doi.org/10.1029/GL010i004p00249

Stranges, D., Yang, X., Chesko, J. D., & Suits, A. G. (1995). Photodissociation of ozone at 193 nm by high-resolution photofragment translational spectroscopy. *The Journal of Chemical Physics*, *102*(15), 6067–6077. https://doi.org/10.1063/1.469341

Summers, M. E., Conway, R. R., Siskind, D. E., Stevens, M. H., Offermann, D., Riese, M., et al. (1997). Implications of satellite OH observations for middle atmospheric H_2O and ozone. *Science*, *277*(5334), 1967–1970. https://doi.org/10.1126/science.277.5334.1967

Thomas, R. J., Barth, C. A., Rusch, D. W., & Sanders, R. W. (1984). Solar Mesosphere Explorer near-infrared spectrometer: Measurements of 1.27-μm radiances and the inference of mesospheric ozone. *Journal of Geophysical Research*, *89*(D6), 9569–9580. https://doi.org/10.1029/JD089iD06p09569

Toumi, R., Houston, P. L., & Wodtke, A. M. (1996). Reactivate O_2 ($v \geqslant 26$) as a source of stratospheric O_3. *The Journal of Chemical Physics*, *104*(2), 775–776. https://doi.org/10.1063/1.471642

Wang, S., Li, K. F., Pongetti, T. J., Sander, S. P., Yung, Y. L., Liang, M. C., et al. (2013). Midlatitude atmospheric OH response to the most recent 11-y solar cycle. *Proceedings of the National Academy of Sciences*, *110*(6), 2023–2028. https://doi.org/10.1073/pnas.1117790110

Waters, J. W., Froidevaux, L., Harwood, R. S., Jarnot, R. F., Pickett, H. M., Read, W. G., et al. (2006). The earth observing system microwave limb sounder (EOS MLS) on the Aura satellite. *IEEE Transactions on Geoscience and Remote Sensing*, *44*(5), 1075–1092. https://doi.org/10.1109/tgrs.2006.873771

Wiensz, J. T. (2005). *Ozone retrievals from the oxygen infrared channels of the OSIRIS infrared imager*. (Doctoral dissertation. University of Saskatchewan). Retrieved from http://hdl.handle.net/10388/etd-07042005-095222

Williamson, D. L., & Rasch, P. J. (1989). Two-dimensional semi-Lagrangian transport with shape-preserving interpolation. *Monthly Weather Review*, *117*(1), 102–129. https://doi.org/10.1175/1520-0493(1989)117<0102:tdsltw>2.0.co;2

Zarboo, A., Bender, S., Burrows, J. P., Orphal, J., & Sinnhuber, M. (2018). Retrieval of O_2 ($1\ \Sigma$) and O_2 (1Δ) volume emission rates in the mesosphere and lower thermosphere using SCIAMACHY MLT limb scans. *Atmospheric Measurement Techniques*, *11*(1), 473–487. https://doi.org/10.5194/amt-11-473-2018